Study of a C-Wing Configuration for Passive Drag and Load Alleviation

S.N. Skinner* and H. Zare-Behtash

School of Engineering, University of Glasgow, Scotland G12 8QQ, UK

Abstract

Non-planar wing configurations are often hypothesised as a means for improving the aerodynamic efficiency of large transport aircraft; C-wings may have the ability to exploit and unify drag reduction, aeroelasticity, and dynamics and control but their capacity to do so is ambiguous. The purpose of this work is to provide an experimental demonstration with the aim of verifying the C-wing configurations practical application. Thus, the main objective of this investigation is to quantify the C-wing's ability for drag and load alleviation relative to a planar wing of equivalent wingspan, lift, and root bending moment at $Re = 1.5 \times 10^6$. Surface clay flow visualisations have been used to provide insight into the flow over the wing surface. Aerodynamic performance metrics show that despite the C-wing operating with a 19.1% higher wing wetted area, a peak total drag reduction of 9.5% at $\alpha = 6^o$ is achieved in addition to a 1.1% reduction in the wing root bending moment for equivalent lift. Force platform measurements in combination with laser vibrometry enabled a detailed understanding of the vibrational characteristics between the model and the wind tunnel. It is shown that the C-wing can passively attenuate buffet induced vibrations of the main-wing by up to 68.6% whilst simultaneously reducing total drag without a significant increase in wing weight or root bending moment.

*Corresponding Author: s.skinner.1@research.gla.ac.uk

Nomenclature

AR	Aspect Ratio
a	Non-dimensional Distance from Elastic Axis to Inertial Axis, m
b	Wingspan, m
C_D	Drag Coefficient
C_L	Lift Coefficient
C_{L_α}	Lift Curve Slope
$C_{m_{pitch}}$	Pitching Moment Coefficient
$C_{m_{RBM}}$	Root Bending Moment Coefficient
C_{m_α}	Pitch Stiffness
c	Local chord, m
$\bar{c}$	Mean Aerodynamic Chord, m
$c_{m,0}$	2-Dimensional Pitching Moment Coefficient
EI	Flexural Rigidity, $Pa\,m^3$
e	Non-dimensional Distance from Elastic Axis to Aerodynamic Centre, m
F	Force, N
f	Frequency, s^{-1} [Hz]
GJ	Torsional Rigidity, Nm
g	Acceleration Due to Gravity, ms^{-2}
h	Altitude, m
K	Stiffness, Nm^{-1}
L	Lift, N
M_∞	Mach Number
m	Mass, kg
N	Normal Load Factor, $[L/mg]$
q	Dynamic Pressure, kg
q_∞	Dynamic Pressure, Nm^{-2} [Pa]
R	Damping of Absorber System
R_e	Reynolds Number
S	Wing Area, m^2
t	Time, s

U	Free-stream Velocity, ms^{-1}
X	Displacement of Mass, m
α_o	Angle of Attack, deg
α_{eff}	Effective Angle of Attack, deg
δ^*	Boundary Layer Displacement Thickness
ζ	Damping Coefficient
θ	Amplitude of Vibration
θ	Torsion, Nm
θ_E	Elastic Deformation, deg
Λ	Sweep Angle, deg
λ	Taper Ratio
Φ	Phase
ω	Wingtip deflection, m
ω_d	Damped Natural Frequency, $rads^{-1}$
ω_n	Undamped Natural Frequency, $rads^{-1}$

Subscript

AM	Amplitude Modulation
av	Average
mw	C-wing Main-Wing
sw	C-wing Side-Wing
tw	C-wing Top-Wing
o	Initial State

I. INTRODUCTION

Between now and 2030, there is an estimated global demand for approximately 27,000 new passenger aircraft, potentially worth up to $3 trillion. These aircraft must comply with strategic research agendas developed by the Advisory Council for Aeronautics Research in Europe (ACARE) which aims to enforce strict emission targets by 2050 - CO_2 emissions per passenger kilometre to be reduced by 75%, NO_x emissions by 90% and perceived noise by 65%, all relative to the year 2000[1]. Similarly, the International Civil Aviation Organisation (ICAO) in conjunction with the Federal Aviation Administration (FAA) and the National Aeronautics and Space Administration (NASA) have goals to mature fuel efficient technologies by 2030 in order to meet the same targets as ACARE by 2050[2]. The impact of aviation on the environment is now a main driving factor affecting the deign of future aircraft[3].

In the cruise phase of large transport aircraft, typically 90% of total flight time, the induced drag is relatively lower than the parasitic drag but still contributes 40% to 45% of the total drag budget[4,5]. According to Airbus, a 1% reduction of the total drag for an A340 aircraft operating over long ranges saves 400,000 litres of fuel and consequently 5000kg of noxious emissions per year[6]. If this drag reduction where to be directly correlated to induced drag lower noise emissions would also be achieved. In fact, the trend of wing design specification for commercial transport aircraft over the last 70 years has been to increase the aspect ratio and flexibility (reducing weight) such that more optimal lift distributions (and so lift-to-drag ratios) can be reached. In the same time period commercial interest in non-planar wingtip devices (winglets), whether purpose designed or retrofitted to older fleets, to passively reduce the wing induced drag in take-off, climb, cruise, and decent phases (for a fixed wingspan) is evident[7,8]. However, the lift distribution of today's modern aircraft are already so tightly optimised for compromise between aerodynamic loading, structure, physical size, stability and control, safety , *etc.*, any significant reductions of induced drag cannot be easily obtained, and indeed, there have been several high-fidelity optimisation strategies that strive to further optimise conventional planar wings[9–11].

A potential step forward in air transportation is the introduction of new disruptive technological advancements, which may result in unconventional aircraft configurations[12–14]. Non-planar wing configurations have been widely recognised as a means of reducing total drag compared to conventional planar wing systems of the same span and lift[8]. A number

of unconventional configurations have so far been proposed including the blended-wing-body[15–17], C-wings[18], polyplane, ring wings[19], box wings[20], and joined wings[21–23], including strut- and truss-braced wings[24–26], however, very few exploratory experimental investigations have been conducted on such configurations. In fact, the box wing arrangement among all non-planer configurations was shown by Prandtl[27] to offer the *'best wing system'*, achieving the minimum possible induced drag for a given lift and height-to-span ratio[28].

C-wings have been considered a compromise between a box wing and a winglet; theoretically providing a reduction in the induced drag that approaches that of the closed box wing[14,29–31] arrangement whilst additionally reducing the viscous drag penalty incurred by large wetted areas[32,33]. The C-wing and box wing have also been recognised to have the potential to replace the conventional horizontal stabiliser to provide pitch control[18,34]. However, owing to large and heavy wingtip extensions, the C-wing is inherently sensitive to structural and aeroelastic issues; they are not closed systems like box wing arrangements which are, by comparison, much stiffer as the upper wing is fixed. Despite the aeroelastic concerns C-wings are seemingly prone to, conceptually the auxiliary lifting surface at the main-wing wingtip could be used to introduce substantial damping to modes of vibration; the characteristics of such a design is not obvious.

In consideration of aerodynamic properties alone, Gage[29] identified the C-wing configuration as an optimal solution while attempting to minimise the induced drag of a planform with fixed lift, span and height. Slingerland and Verstraeten[35] used a low-fidelity potential flow model with a drag-free wake to investigate the drag characteristics of optimally span-loaded planar wings, wings with winglets and C-wings. They concluded that with a constrained wingspan, winglets were able to provide drag reductions on the order of 5%, but no significant advantages were found using C-wing configurations. Ning and Kroo[36] conducted a similar investigation taking into account the area-dependant weight, effects of critical structural loading, and stall speed constraints. They concluded that C-wings achieved a lower net drag compared to winglets for a constant positive pitching moment about the aerodynamic centre, especially for wing planforms with span constraints and low sweep. Looking at aeroelastic design trade-offs, Jansen et al.[33] used a medium-fidelity aerostructural panel code approach to show that for maximum induced drag efficiency a box wing configuration was optimal. When compensating for viscous drag effects alone the C-wing configuration was preferred. However, when structural considerations were taken into account, the C-wing

and box wing configurations were found to add more structural weight than their respective drag reduction potential could compensate for; *i.e.* the reduction in induced drag was not worth the gain in structural weight.

Gagnon and Zingg[37] later performed high-fidelity aerodynamic shape optimisation for several non-planar aircraft concepts: a blended-wing-body with C-wings, a box wing, and a high-aspect ratio strut-braced wing. They identified that C-wings provided much greater span efficiencies under optimal loading, however encountered difficulties when optimising the C-wing. By only accounting for variation in the C-wing's horizontal extension span and dihedral, at a fixed height and stagger, the configuration could not be properly optimised. The optimiser attempted to unfold the C-wing in favour of a winglet of increased length. Therefore, the authors conclude that C-wings do not appear to offer any significant benefits over winglets but do point out that more research is needed to confirm this as C-wings offer the opportunity for tailless aircraft with substantially reduced total wetted areas.

Bauhaus Luftahrt[38–40] numerically investigated the development of a C-wing configuration designed for a tailless electric passenger aircraft. The concept was suggested to be able to achieve pitch control and trimmed flight, but the ability to achieve induced drag reduction while maintaining pitch stability requires more evidence. Airbus[41] has also shown interest in the C-wing due to its ability to exploit and unify drag reduction, aeroelasticity, and flight dynamics and control. It is suggest that longitudinal stability requirements cannot be met if significant reductions in induced drag are perused; the performance improvement due to induced drag reduction was lost due to the increased wing weight necessary to provide control authority. Aeroelastic design constraints of the C-wing, to avoid flutter and divergence, were able to be met in the optimisation design problems when provisions where made to not use the top-wing to provide longitudinal control authority. This reduced the weight of the outboard wing section. Potential aerodynamic benefits of C-wings have also been realised by Suresh et al.[42], who used a commercial computational fluid dynamics (CFD) package to compare a planar wing with, and without, an arbitrary C-wing extension. Inviscid simulations with a Mach number of 0.85, and Reynolds number of $\approx 10^8$, conclude that the lift-to-drag ratio increased for low angles of attack, however this is the result of large increases in both lift and drag. Parasitic drag, wing loading and/or moments were not taken into account in this study. Following on from this work Gobpinaath et al.[43] present a combined numerical and experimental investigation of C-wings at low Reynolds numbers (

$\approx 1.8 \times 10^5$). They observed that the C-wing can achieve improved lift-to-drag ratios in the range of $2 \leq \alpha \leq 6$ compared to an equivalent planar wing.

Conclusions and understanding of the performance of C-wing configurations, whether positive or negative, are conflicting. Numerical investigations vary depending on the specific design problem considered and the fidelity/scope of the physics models used. This is compounded by the distinct lack of experimental wind tunnel data. Thus, the objective of this work is to provide an experimental demonstration with the aim of verifying the C-wing configurations practical application. The wind tunnel tests are designed to be an exploratory *'proof of concept'* study. This is achieved by considering aerodynamic metrics of the C-wing relative to a planar wing of equivalent wingspan, lift, and root bending moment while considering how the global flow over the main-wing is effected by the addition of the C-wing. Furthermore, efforts have been made to design the wing configurations such that bend-twist deformations were decoupled when aerodynamically loaded, resulting in near pure bending of the wing. This characteristic enabled the assessment of buffet induced vibration by simplifying the dominant vibration of the main-wing to bending modes alone.

II. THE C-WING LAYOUT

The C-wing configuration is a three element wing system consisting of a side-wing and top-wing mounted at the wingtip of the main-wing, as shown in figure 1.

C-wings differ from other multi-element configurations (such as a bi-plane or canard) as the secondary surface is designed to produce a down force, thereby acting against useful lift[14]. Typically non-planar wing configurations attempt to reduce induced drag contributions by scheduling the loading on each of the lifting surfaces, the C-wing achieves drag reduction via two mechanisms: 1) alteration of the main-wing load distribution by promoting a less pronounced decrease in local lift at the main-wing wingtip; and 2) forward tilting of the lift vector of the top-wing where the main-wing's down-wash is exploited to produce a thrusting effect. If designed appropriately, winglets, and indeed all non-planar wingtip variants, can be made to show aerodynamic advantages when compared to conventional designs but often fail as they usually lead to structurally heavier wings with detrimental increases in parasitic drag.

The optimal loading condition indicated in figure 1 indicate that the circulation of the

main-wing is carried onto the side-wing, acting much like a winglet, thus loaded inward toward the fuselage[14]. The circulation is then further extended onto the top-wing producing a net down-loaded surface for minimum induced drag at a fixed total lift and wingspan. The goal of minimising the induced drag of the system requires the gradients of circulation, where possible, to be minimised[27]. Conventional planar wings shed strong vortices at the wingtips and the circulation tends to zero. Hence, distributing the vorticity in the wake over an effectively longer wingspan would reduce the wake sheet intensity (weaker vortices shed), in addition to moving the wingtip vortices closer together than that for a conventional wing, accelerating the breakdown of the wake system[18]. The down-loading of the top-wing surface will naturally have an effect on the structural weight, performance and control, and may provide a means of stability that is less effected by the main-wing down-wash such as conventional horizontal stabilisers.

III. EXPERIMENTAL SET-UP

A. Experimental Facility

The de Havilland National Wind Tunnel Facility (dH) is an atmospheric low-speed closed return wind tunnel circuit. The working section has an octagonal cross-section of $2.65m$ width, $2.04m$ height, and $5.64m$ length with a contraction ratio of $5:1$. The corner fillets are arranged to enable the test section's cross sectional area to expand from inlet to outlet compensating for boundary layer growth and offset the resulting longitudinal static pressure gradients which contribute to horizontal buoyancy effects.

Surface clay flow visualisations have been used to provide insight into the time-averaged flow structures over each wing configuration at a given angle of attack. The clay flow formulation consisted of fine white Kaolin clay suspended in paraffin. Results have been obtained by the following procedure: 1) setting the model angle of attack; 2) evenly applying the clay mixture to the wing leading edge; 3) operating the wind tunnel from zero velocity to the operational flow regime in a relatively short time (≈ 4 seconds), and recording continuously (with a Phantom v341) to monitor the progressive movement of the clay; 4) continued operation of the wind tunnel until clay mixture is dry (≈ 12 minutes). Colour images were taken using a Canon SLR camera, model EOS-450D with 12 mega-pixel resolution.

An Ate AEROTECH $2m$ diameter turntable has been used for model position; capable of providing 360^o motion at $5^o s^{-1}$. The yaw of the turntable was used to control the angle of incidence of the model with a position accuracy is $\pm 0.005^o$. Aerodynamic coefficients have been assessed using a AMTI OR6-7 1000 series force platform which was housed in the centre of the turntable beneath the tunnel floor, as shown in figure 4. The force platform measures the three orthogonal force components along the X, Y, and Z axes, and the resulting moments about each axis. Measurement accuracy is $\pm 0.25\%$ of the applied load on the respective output. Each output was recorded at $2kHz$ over $20s$ for static conditions only.

For collaborative characterisation of the model vibration/dynamic loading recorded by the force platform, and a Polytec PDV-100 digital laser vibrometer was employed for non-contact single degree of freedom velocity measurements. The point vibrometer made it possible to isolate certain frequencies and their sources; all measurements were sampled over $26.5s$ at a frequency of $10kHz$, achieving a resolution of $39mHz$. No filtering was applied at data acquisition; if used, any post-processing filters have been specified with results. As the vibrometer only provided data at a single position phased vibration, such as the wing torsional modes, cannot be assessed with complete certainty, however based on the model design and experimental observations of buffet induced vibration, fundamental mode types can be estimated.

B. Semi-Span Model

The planar wing, shown in figure 2(a), is analogous of a typical mid-sized transport commercial aircraft wing topology, representing a 10%-scale model. The fuselage is a generic axisymmetric half-body fairing. A modular design enables the outboard wing section to be freely changed, with the C-wing arrangement shown in 2(b). The primary function of the C-wing attachment is to reduced the total drag of the semi-span model (hence, reduction of induced drag must be greater that gains in parasitic drag) relative to the planar wing system. In this study, only information of the total drag is available, hence independent variations of the parasitic and induced drag cannot be assessed. To reduce the complexity for both the experimental campaigns and model manufacture, all wing sections are untwisted with a constant NACA $63_1 - 412$ aerofoil section. Due to lack of wing twist (washout) sub-optimal lift distribution over the wing, regardless of wingtip arrangement, is expected. Furthermore,

while the C-wing may achieve a total drag reduction, is it unlikely that it will provide the optimal reduction of induced drag.

Figure 3 illustrates an exploded view of the semi-span model and how it interfaces with the force platform. Wing and fuselage sections are constructed from polyurethane foams with an aerodynamically smooth finish of surface roughness $< 0.1\mu m$. The main-wing section connects through the fuselage's aluminium spine to the steel balance interface. The steel balance interface is mounted centrally to the force platform's electromechanical centre, which is located at the centre of the turntable. Thus, the electromechanical centre and the model's mounting shaft of the steel balance interface are fixed to the pitch axis. The pitch axis is however not geometrically fixed to the model; the steel balance interface connects to the spine in such a way to allow $210mm$ longitudinal translation. This capability serves two purposes: 1) aligning the model's centre of gravity with the pitch axis, thus also accommodating longitudinal changes to the centre of gravity position; and 2) the model translation can be used to accommodate limitations in optical access. It is noted in this study that the change in position of the model's centre of gravity between wingtip configuration is negligible. The interchangeable wingtip extensions to the main-wing are also shown in figure 3, where the wingtip locking point connects the desired wingtip arrangement directly to the elastic axis of the main-wing.

A schematic diagram of the semi-span of the model with each wingtip arrangement used in this study is given in figure 4, with relevant wing specifications and scaling information listed in table I. The Reynolds number (Re) is based on the wing's mean aerodynamic chord (MAC) with atmospheric properties taken from Anderson[44].

Evident from figure 4, the semi-span model does not utilise the transitional peniche extrusion at the model's mid-plane cross section, instead a stand-off gap is employed. Skinner and Zare-Behtash[45] showed that this has the advantage of preventing the development of a horseshoe vortex in-front of the model, at the peniche wall juncture. In this study, the stand-off gap is scaled to four-times the empty wind tunnel working section boundary layer displacement thickness (δ^*) at the pitch axis (located at the mounting shaft) of the model[45]. Figure 4 additionally indicates the position of the mode's the centre of gravity aligned with the mounting shaft as previously discussed. Relative to the planar wing, the C-wing has an 0.87% reduced wingspan also reducing the aspect ratio of the main-wing surface by 1.42%, a 0.16% increased 'useful lift' wing area, and an increased wing wetted area of 19.1%.

TABLE I: Wing parameters.

	Conventional full-scale	Planar	C-wing
Mach Number (M_∞)	$\approx 0.78 - 0.8$	0.145	0.145
Reynolds Number (Re)	$\approx 10^9$	1.5×10^6	1.5×10^6
Altitude (h) $[m]$	$\approx 10972.8(36,000ft)$	0	0
Dynamic Pressure (q_∞) $[Pa]$	≈ 10107.04	≈ 1531.25	≈ 1531.25
(Main) Wing Area (S) $[m^2]$	$\approx 65 - 90$	0.5717	0.5726
MAC ($\bar{c}$) $[m]$	$\approx 4 - 5$	0.44	0.44
Wing Semi-Span ($b/2$) $[m]$	$\approx 17 - 19$	1.50	1.487
Taper Ratio (λ)	≈ 0.2	0.21	0.174
Aspect Ratio (AR)	$\approx 4 - 4.5$	4.12	4.06

Each wing arrangement was designed using a in-house developed population structured genetic algorithm (sGA) which utilised an experimentally validated unsteady vortex-ring panel code[46]. This provided an effective design tool to ensure experimental constraints and design criteria could be met while maintaining characteristics of each wing arrangement. Thus, the design of the two wings are related in their design architecture with the same specifications and underlying physics, additionally facilitating a C-wing design that is not arbitrary. The planar wing's design specification was dictated by criteria adhering to the test facility limitations which placed restrictions on wing sizing (relative to the wind tunnel working section), and maximum feasible force/moments dictated by the force platform range. The latter placed constraints on the maximum measurable root bending moment, while the algorithm's objective minimised the induced and parasitic drag of the wing independently. The sGA also designed the wing such that the aerodynamic centres of the planar wing aligned with the 34% chord along the span for alignment with the physical wing's elastic axis.

For the C-wing, the sGA was tasked to redesign the outboard 26% of the planar wing wingspan in the design of the C-wing wingtip; this preserving the main-wing section between arrangements as shown in figures 3 and 4. The C-wing configuration was designed to reduced total drag of the system while maintaining an equivalent (or smaller) wingspan and root bending moment for the same lift relative to the planar wing configuration. This enables

a confident comparison of the arrangements with regards to the aerodynamic performance of the overall wing system[7]. The successful application of any non-planar wing system for improving the aerodynamic efficiency depends entirely upon the ability to construct the wing system such that a sufficiently low root bending moment and parasitic drag is maintained, relative to the equivalent planar wing system[12]. It is important to emphasise that both configurations in this study are not truly optimal, but are optimal given the allowable design space and experimental constraints.

IV. AEROELASTIC WING DEFORMATION

Wings are prone to distortion when exposed to aerodynamic loads from which structural distortions modify the aerodynamic loading, which then feedback into further structural distortions. The main-wing section, indicated in figures 3 and 4, has been designed to provide, as closely as possible, pure bending deformation in order to simplify the wing analysis. This is typically achieved though passive aeroelastic tailoring[47,48]. However, in the present study aeroelastic tailoring of the wing structure has not been adopted as the wing components are manufactured from polyurethane foam, an isotropic material. Thus, to achieve decoupled bend-twist deformation, the moments acting around the main-wing elastic axis have been balanced. Furthermore, this approach inherently provides confidence that structural failure from torsional divergence or flutter will not occur.

Consider the elastic deformation of a swept finite planar wing with aerodynamic centres over the wingspan, with elastic and inertial axes as presented in figure 5. Wing cross section **A-A** illustrates the distances/moment arms which can drive aeroelastic bend-twist coupling: the aerodynamic coupling, ec, and the inertial coupling, ac. To observe the static aeroelastic characteristics of such a configuration, a distributed aerodynamic loading would act as a distributed load through, and a distributed twisting moment about, the elastic axis. Thus, the total translation at elemental section, δz, can be described as the combination of rotations caused by elastic twist, θ' from torsion about the z' axis, and the wing bending $\frac{d\omega}{dz'}$, where ω is the wing's bending about axis x'. The effect of elastic deformation, θ_E, over the wingspan thereby modifies the wing root angle of attack, α_0, across the wingspan. Thus,

the effective angle of attack α_{eff} along the span of a swept wing is described as:

$$\alpha_{eff}(z) = \alpha_0 + \underbrace{\theta'(z')cos\Lambda - \frac{d\omega(z')}{dz'}sin\Lambda}_{\theta_E=\text{Elastic deformation}} \tag{1}$$

Consider the static aeroelastic deformation of the wing, *i.e.* the interaction of aerodynamic loading from a steady flow and the associated elastic deformation of the wing structure. This type of interaction is characterised as being insensitive to rates of change and accelerations of the structure. Hence, by using fundamental aeroelastic theory the effect of aerodynamic coupling on bend-twist deformation is considered. The total elastic deformation over the wingspan at elemental strip, δz, of infinitesimal thickness, can be described by two equilibrium equations: one for torsional moment equilibrium, and one for bending force equilibrium. Such equations can be expressed as[49]:

Torsional moment equilibrium:

$$\begin{aligned} &\frac{d^2\theta'}{dz'^2} + \frac{qec\frac{\partial C_l}{\partial\alpha}}{GJ'}\theta' cos^2(\Lambda) - \frac{qec\frac{\partial C_l}{\partial\alpha}}{GJ'}\frac{d\omega}{dz'}sin(\Lambda)cos(\Lambda) \\ &= -\frac{1}{GJ'}[qec\frac{\partial C_l}{\partial\alpha}\alpha_0 cos(\Lambda) + qc^2 c_{m0}cos^2(\Lambda) - Nmgac] \end{aligned} \tag{2}$$

Bending moment equilibrium:

$$\begin{aligned} \frac{d^4\omega}{dz'^4} + \frac{qc\frac{\partial C_l}{\partial\alpha}}{EI'}\frac{d\omega}{dz'}sin(\Lambda)cos(\Lambda) - \frac{qc\frac{\partial C_l}{\partial\alpha}}{EI'}\theta' cos^2(\Lambda) \\ = \frac{1}{EI'}[qc\frac{\partial C_l}{\partial\alpha}\alpha_0 cos(\Lambda) - Nmg] \end{aligned} \tag{3}$$

Gravity conventionally acts in the $-y$ direction relative to the wing presented in figure 5, but for the current experimental set-up gravity acts in $+z$. It is observed analytically that when $ec \to 0$, $ac \to 0$, and $g = 0$, bend-twist coupling of the wing is almost entirely mitigated, except from the inherent contribution from wing sweep. Thus, equations 2 and 3 reduce to:

Torsional moment equilibrium:

$$\frac{d^2\theta'}{dz'^2} = -\frac{1}{GJ'}[qc^2 c_{m0}cos^2(\Lambda)] \tag{4}$$

Bending moment equilibrium:

$$\begin{aligned} \frac{d^4\omega}{dz'^4} + \frac{qc\frac{\partial C_l}{\partial\alpha}}{EI'}\frac{d\omega}{dz'}sin(\Lambda)cos(\Lambda) - \frac{qc\frac{\partial C_l}{\partial\alpha}}{EI'}\theta' cos^2(\Lambda) \\ = \frac{1}{EI'}[qc\frac{\partial C_l}{\partial\alpha}\alpha_0 cos(\Lambda)] \end{aligned} \tag{5}$$

It is highlighted that as gravity is not acting in the conventional direction relative to the wing orientation (but along the wing span), the wing's inertial axis will persist as the wing has mass, but the effects of which will be negligible. Hence, there exists combinations of the aerodynamic and inertial couplings that aeroelastic theory would analytically indicate a decoupled bend-twist deformation. If the inertial axis coincides with the elastic axis, $ac \to 0$, and similarly, if the aerodynamic centre coincides with the elastic axis, $ec \to 0$, then bending and torsion deformation will be decoupled[50]. With the line of aerodynamic centres aligned with, or aft of, the elastic axis the wing will remain statically stable at all speeds and a torsionally divergent state will not be reached[51–53]. Furthermore, if both coupling terms tend to zero, indicating coincidence of the three axes, flutter (due to the 90^o phase shifted coupled oscillation wing twist-bending) cannot occur at any velocity[49]. Fung[51] indicates that if alignment of the axes is achieved, oscillatory bending modes of the wing will remain aerodynamically stable and that purely translational flutter is impossible without the phase relationship with torsional modes.

Hence, alignment of the aerodynamic centres along the wingspan with the elastic and inertial axis will result in pure bending elastic deformation, ω, with aerodynamic loading as indicated in figure 6. Figure 6 also shows the alignment of the three axes for each wingtip arrangement, where each wingtip connects to the main-wing such that no discontinuities in the axes alignment arise.

It follows that the planar and C-wing wingtip translation and rotation from aerodynamic loading at $Re = 1.5 \times 10^6$ for several angles of attack have been inferred using an in-house 2-dimensional direct imaging correlation (DIC) technique. Wingtip translation measurement sites are indicated in figure 6. DIC is a non-intrusive optical approach for measuring structural deformation, in which digital photographs (provided by a Phantom v341 digital high speed, 4 Megapixel camera with 2560×1600 pixels) of the structure at different stages of deformation are compared. A MATLAB script was used to analyse digital images of the unloaded and loaded wing arrangements, which used calibration images to relate the camera CMOS chip co-ordinate system with the spatial co-ordinates of the object plane of interest. This provides the necessary transfer functions required to convert pixel displacements to physical structural deformations. The DIC results from the wingtip translations for each wing arrangement are presented in figure 7. Negative angles indicate leading edge down rotation.

Figure 7 indicates that each wing arrangement show similar bend-twist behaviour at the wingtip. Peak wingtip deflections of $\omega/\bar{c} = 0.2065$ and 0.2259, for the planar and C-wing respectively, occur at $\alpha = 14^o$. The negative trend of the wingtip rotation with angle of attack suggests that the aerodynamic centres along the wing lie slightly aft of the elastic axis. The effect of the C-wing's top-wing is seen to be responsible for modifying the wingtip translation. At low angles of attack ($\leq \alpha = 8^o$) the top-wing is down-loaded (opposing main-wing lift) and therefore reduces the wingtip translation, as shown in figure 7(a). Similarly, figure 7(b) illustrated that this down-loading of the top-wing enforces a nose up pitching moment which increases the wingtip twist angle. At angles of attack $> \alpha = 8^o$, figures 7(a) and (b) suggest that the C-wing becomes positively loaded (contributing to main-wing lift) therefore increasing the wingtip translation, and now imposing a nose down pitching moment at the wingtip relative to the planar wing.

V. RESULTS AND DISCUSSION

A. Surface Clay Flow Visualisations

Time-average surface clay flow visualisations for the planar and C-wing main-wing at $\alpha = 0^o$, 8^o and 14^o are shown in figure 8(a) and (b), respectively; the flow direction and direction of gravitational force have been indicated. Qualitatively, surface flow structures arising from attached/separated flows, stall cell formations, model surface imperfections, and horseshoe vortex interactions can be examined. The flow over each wing's upper surface at $\alpha = 0^o$, shown in figure 8 (a) and (b) for both the planar and C-wing main-wing respectively, is fully attached with no inexplicable deviations from the free stream flow direction. Vortical wake structures in the order of $4mm$ are visible immediately down stream of all six wingtip locking pins in addition to larger flow disturbances caused by the wingtip joint, however these features are deemed to have a negligible effect on the overall flow field.

With increasing the model's angle of incidence to $\alpha = 8^o$, clear outboard separation is noted for both the planar and C-wing. Outboard stall of the untwisted swept wing, while detrimental to performance, is expected. The stall lines in each wing configuration share similar profiles; the only distinctive difference is that the C-wing's stalled region progresses onto the side-wing. Interference patterns due to the locking pins and wingtip joint are

indistinguishable from the $\alpha = 0^o$ case. At the wing root/fuselage juncture, streamline deviations show evidence of induced flow from a horseshoe vortex; the horseshoe vortex root is located at the leading edge (LE) of the wing root. Furthermore, both wing configurations show evidence of light LE separation bubbles over the span of the wing.

At $\alpha = 14^o$ there are consistent stall characteristics between the planar wing and C-wing's main-wing. Surface flow visualisations for both configurations show the development of three stall cells; these have been labelled P1, P2, and P3 for the planar wing at $\alpha = 14^o$ shown in figure 8(a), and C1, C2, and C3 for the C-wing at $\alpha = 14^o$ shown in figure 8(b). Soon after the wind tunnel reaches stable operating conditions, the progressive accumulation of the clay flow mixture forms along the stall front, and begins collecting in these stall cells. The immediate build-up of clay in the location of the stall cells suggests that the stall cell locations are immediately realised in explicit locations with no-large spacial fluctuations. The abundance of the clay in the stall cell is translated from the recirculation region formed by the buckling of the separation front. It is further noted that a consistent modification of the clay flow streamlines from their otherwise straight path is seen upstream of the separation as they blend together into the separation front.

The wing-to-wingtip joint appears to act in a similar manner to a vortex generator, in that the resulting turbulence promotes attached flow which seems to divide a larger stall cell into two as seen in figure 8(a) and (b) at $\alpha = 14^o$. This moves a smaller stall cell towards the wingtip, labelled P1 and C1, from a much larger stall cell extending from the wingtip join down to the yehudi wing break, P2 and C2, which are indistinguishable from one another. This phenomenon occurs identically for both the planar and C-wing, however the stall cell C1 located towards the C-wing main-wing tip appears larger relative to P1. This is likely caused by the stall progressing onto the C-wing's side-wing, which has the effect of elongating stall cell C1.

Stall cell P3 for the planar wing and C3 for the C-wing, located at the wing TE near the wing root, show similar interactions with the wing root horseshoe vortex which forces reattachment inboard of P3/C3. The induced flow from the horseshoe vortex, coupled with boundary layer thickening inboard of the yehudi, is seen to have the effect of sharply turning the inboard wing flow down toward stall cell P3/C3 as suggested by the streamlines and the build-up of clay. From the experimental observations and the development of the surface streamlines with time, it is assumed that forces due to gravity are negligible, and that fluid

dynamic shear forces from the flow on the clay are dominant.

Additionally, common between both configurations at $\alpha = 14^o$ is the formation of a LE separation bubble over most of the wingspan as indicated in figure 8 (a) and (b). As the wing is untwisted the separation bubble forms a straight line along the LE. At the operational Reynolds number regime of 10^6 a short separation bubble is expected to occur as the very initial flow in-contact with the wing is laminar. Since a laminar boundary layer is incapable of coping with anything but a very slight adverse pressure gradient, the flow almost immediately separates. The separated flow then transitions to turbulence, entraining fluid and re-attaching forming a turbulent boundary layer. In other words, the laminar LE separation bubble represents the transmission-forcing tripping mechanism to a turbulent boundary layer. At the operational Reynolds number, and angles of attack of interest, this separation bubble will remain $1 - 2\%$ of the local chord and will not greatly affect performance. The formation and structure of laminar LE separation is described in detail by Wallis[54] and Lissaman[55].

B. Force and Moment Measurements

Changes in lift, drag, pitching moment about the model's centre-of-gravity/pitch axis, and the wing's notional root bending moment are presented in figure 9, illustrating the behaviour of the C-wing relative to the planar wing. All measurement have been corrected for solid-body blockage (Planar wing: 4.9% at $\alpha = 14^o$; C-wing: 5.2% at $\alpha = 14^o$), wake blockage, and horizontal buoyancy using methods presented by Barlow et al.[56]. The force and moment data presented have been calculated with a confidence level of 98% with a margin of error less than 1% for each datum. The model has only been operated in the pre-stall region to prevent damage to the wing due to high flexibility in bending.

In order to draw comparisons between the two wing configurations, in which one is expected to achieve some reduction of the induced drag, it is common practice to maintain equivalent wing lift coefficient without any gain in root bending moment[7]. Typically, any reductions of induced drag are offset by the increase in the root bending moment; Takenaka et al.[57] showed a linear correlation between winglet span length, induced drag reduction, and increases in root bending moment. Figures 9 (a) and (d) show that the lift coefficient and notional root bending moment coefficients match closely for the angles of attack tested. From

flow visualisations shown in figure 8 it is understood that each wing configuration stalls near the wingtip spreading inboard. This agrees with the reduction of the root bending moment at higher angles of attack, shown in figure 9(d), where corresponding data points in figure 9(a) only loose small amounts of lift.

The linear portion of the lift curve slope for the planar wing is $-5 \leq \alpha \leq +7$, while the linear portion of the C-wing is $-5 \leq \alpha \leq +5$; the resulting lift curve slope, C_{L_α}, is 0.100 and 0.104 respectively. At negative angles of attack, the C-wing's top-wing angle of attack becomes increasingly more positive, and so more strongly down-loaded. Hence, the increasingly down-loaded top-wing reduces the wing's net lift relative to the planar wing, as evident in figure 9(a), also resulting in the reduced root bending moment seen in figure 9(d). The down-loaded top-wing is also alters the pitching moment in figure 9(a). The top-wing not only causes a nose up pitching moment for $\alpha \leq -2^o$, but is also seen to maintain a negative pitch stiffness derivative, C_{m_α}, thus implying longitudinal static stability.

Figure 9(b) shows the total drag variation with angle of attack for the planar and C-wing configurations. At angles of attack $\alpha \leq 0^o$ the drag of the C-wing is higher with a maximum total drag increase of 16.6% at $\alpha = -5^o$ due to parasitic drag gains. However, the drag reduction of the C-wing across the positive angle of attack range is clear. Despite the increased wetted area, resulting in higher parasitic drag, the C-wing achieves an average total drag reduction of 7.4% over the $0^o \leq \alpha \leq +14^o$ range. Peak drag reduction is reached at $\alpha = 6^o$, with a 9.5% saving. With further increases in the model's angle of attack, the C-wing begins to entering a condition analogous of T-tail aircraft approaching deep stall. In this condition the main-wing's wake begins to impinge on the top-wing reducing it's effectiveness.

To summarise the tends discussed in the aerodynamic coefficients, figure 10 presents the percentage increase/decrease of the C-wing's aerodynamic coefficient at angle of attack α relative to the planar wing arrangement. It is immediately event that at negative angles of attack, the down-force of the top-wing causes a reduction in lift and root bending moment root bending moment, while increasing total drag. This has the combined effect of also reducing the lift-to-drag ratio. Over positive angles of attack ($0 \leq \alpha \leq +14$) the lift-to drag ratio increases by an average of 8.5%, with a peak increase of 10.67% at $\alpha = 6^o$.

C. Model Vibration

1. *Bump Tests*

The transient response from bump tests for both the planar wing and C-wing arrangements have been analysed to better understand fundamental vibrational characteristics without the influence of wind loading (vibrations from wind tunnel turbulence) and forced wind tunnel vibrations (vibrations related to natural frequencies of the wind tunnel structure). By focusing the laser vibrometer to different measurement locations and bump testing the model, thereby exciting all natural frequencies of the model, measurements of the associated natural frequencies and system damping can be identified. Since the measurements are one-dimensional, the bending and torsional modes cannot be definitively differentiated. However, from the experimental observations dominant the modes are anticipated to be the bending modes typical of swept-wings.

The frequency response evaluated from the main-wing for both wing configurations are shown in figure 11(a), with the bump test response of the C-wing top-wing response shown in figure 11(b). The bump test location, shown in figure 11(a), is located at $z/b = 74\%$ span on the flexural axis of the wing; the flexural axis along the wing is located at 34% of the local chord. The C-wing demonstrates a more complex vibrational system however there is a clear attenuation of the vibration. The bump tests show a 41.2% reduction of the first mode ($7.2Hz$ planar to $5Hz$ C-wing), and a 45.8% reduction of the second mode ($33.5Hz$ planar to $32.1Hz$) in figure 11(a). The C-wing is also observed to introduce a unique low magnitude split-peak within the frequency domain at $8.45Hz$ and $8.98Hz$.

The top-wing extension is suitably positioned for passive vibration absorbency as is it connected via wingtip which will experience the structure's greatest amplitude deflections[58]. Such a design is expected to introduce other peak response frequencies in the structure, typically one bellow and the other above the excitation frequency it suppresses[59,60]. The dominant $7.2Hz$ peak present in the planar wing has been broken down into two smaller frequency shifted peaks in the C-wing configuration ($5.0Hz$ and $12.7Hz$). This behaviour is indicative of the C-wing acting as a dynamic vibration absorber[61–63], absorbing the vibrational energy within a certain frequency interval thereby reducing the dynamic response of the system. The sharpness of the frequency peaks imply that the vibration absorber has

very low damping[61]; a damped/tuned vibration absorber would have characteristically softer peaks.

Considering the bump tests performed directly on the C-wing, the split-peak becomes more predominant as seen in figure 11(b); the bump test location shown in figure 11(b) is located on the C-wing's top-wing wingtip at 34% local chord. Examination of the temporal response from bump tests is displayed in figure 12 and can be used to gain further insight into the split-peak phenomena observed. Main-wing vibrations under bump testing (figure 11(a)) for both the planar and C-wing cases give temporal responses shown in figures 12(a) and (b), respectively. Perceptual segregation of the modal frequencies has been achieved through applications of elliptic bandpass filters which can provide sharp roll-off, helping to isolate frequencies that are close to one another. The overall system reaction to bump tests characteristically resembles the response of an under-damped 2^{nd} order system. This free vibration, due to an initial displacement θ_o, is theoretically described by:

$$\theta(t) = \theta_o e^{-\zeta\omega_n t}\left\{cos\omega_d t + \frac{\zeta}{\sqrt{1-\zeta^2}} sin\omega_d t\right\} \tag{6}$$

Within the C-wing's response an amplitude modulated vibrational mode with a frequency of $8.7Hz$ is observed in figure 12(b). This amplitude modulated response is clearer if the C-wing top-wing is considered directly, this is shown in figure 12(c). This temporal response is, at first glance, made up from two frequencies: 1) an $8.7Hz$ wave, analogous of a carrier wave; and 2) an amplitude modulating wave enveloping the carrier wave at $0.27Hz$. Referring back to figure 11(b), illustrating the bump test of the C-wing top-wing in the frequency domain, it appears that no information concerning the amplitude modulating signal is provided. In the presence of amplitude fluctuations, the ability to detect the modulation of the signal can be masked by the presence of the carrier wave. This effect is known as modulation detection interference (MDI), and by applying full-wave rectification (taking the absolute signal values) to the signal, it is possible to detect the amplitude modulation frequency. Furthermore, as pointed out by Hall and Grose[64], MDI occurs when two carrier waves are grouped into a singular waveform ($8.7Hz$), which brings attention back to the split-peak observed in figures 11(a) and (b).

The two carrier waves, with frequencies of $8.45Hz$ and $8.98Hz$, are identified to be the natural frequencies of the side-wing and top-wing respectively. Considering the physical vibration and interaction between these two components, they are inherently mechanically

coupled. Thus with the two vibrations excited simultaneously, the law of superposition states that the total amplitude is the sum of the vibrational amplitudes at time t. Figure 13 (a) and (b) represent the undamped vibration of the side-wing and the top-wing respectively. Figure 13 (c) shows the superposition of the two vibrations resulting in an interference pattern with amplitude oscillations and a frequency equal to the average of the interfering waves $f_{av} = 8.72$; this phenomena is called beating. The beating pattern is the result of two waves with very similar frequencies which create points of constructive interference and destructive interference as labelled in figure 13. When local maxima of the two waves are $180^o(\pi\ radians)$ out of phase the maxima of one wave cancels the minima of the other (destructive interference); when the local maxima of the two waves have no phase difference, and therefore in phase, the interference pattern shows increased amplitude (constructive interference). The beating pattern can be assessed through consideration of trigonometric identities, leading to equation 7, to aid in the explanation of the beating observed.

$$cos(2\pi f_{tw}t) + cos(2\pi f_{sw}t) = 2cos\Big(2\pi \underbrace{\frac{f_{tw} + f_{sw}}{2}}_{f_{av}} t\Big) cos\Big(2\pi \underbrace{\frac{f_{tw} - f_{sw}}{2}}_{f_{AM}} t\Big) \tag{7}$$

Equation 7 characterises the interference pattern created as the periodic variation in the amplitude (amplitude modulation) of a single carrier wave with frequency f_{av}, where the function modulating the amplitude is occurring at frequency f_{AM}. Intuitively beats occur at twice the amplitude modulating frequency, thus the number of beats per second is the difference in frequency between the two interfering waves:

$$f_{beat} = |f_{tw} - f_{sw}| \tag{8}$$

A summary of the vibrational frequencies associated with the C-wing bump tests and the domain in which they are detectable is summarised in table II.

As the force platform is connected via a steal mounting system through the fuselage symmetry plane the natural frequencies related to the fuselage must also be examined with exclusion of the wind tunnel vibrations. This is necessary to fully understand and explain the frequencies of the forces and moments monitored by the force platform under live experiments. Figure 14 shows the bump test responses observed in the longitudinal axis of the fuselage for both the planar and C-wing configurations. Examination of the figure shows that the effect of different wing configurations is negligible on the frequency spectra observed

	Observed Frequencies				
Detection	f_{sw}	f_{tw}	f_{av}	f_{AM}	f_{beat}
Temporal Domain	√	√		√	
Frequency Domain			√	√	√

TABLE II: Summary of frequencies associated with the C-wing in free vibration and the domain in which they are detectable.

in which there are two distinct frequencies; the low magnitude of the vibrations are due to the high stiffness of the fuselage. The $9.3Hz$ registered is anticipated to be related to the fundamental bending mode of the main-wing structure, previously identified at $7.2Hz$ for the planar wing, and $5Hz$ for the C-wing. It is logical that a frequency shift in the wings fundamental mode is observed between the two measurement locations as they structurally separated by several components of varying material. The $39.9Hz$ frequency is only excited through longitudinal bump tests of the fuselage.

2. Wind tunnel Vibrations

In this study we consider static conditions only. However even under static conditions, wing deformation combined with vibrations will inevitably contribute towards a more dynamic loading detected by the force platform. Previous bump tests enabled the identification of frequencies related to the semi-span model in isolation of the wind tunnel influence. Similarly, it is imperative to understand the frequencies that will be forced onto the model by the wind tunnel by both vibrations in the air and the wind tunnel structure. Figure 15 shows the vibrational frequencies detected by the laser vibrometer in the steel frame supporting the working section of the wind tunnel. The test case here matches the test case for the semi-span model with a Reynolds number of 1.5×10^6 based on the wing MAC.

To achieve this Reynolds number, the wind tunnel fan operates at approximately $615rpm$ $(= 10.25Hz)$ which may drift slightly depending on the air temperature. This frequency is visible in the Fourier transform in figure 15, in addition to a $40.80Hz$ frequency due to the fan having four blades, and a $82.01Hz$ frequency related to the fans section's eight stators. It is noticeable that the vibrations related to the stators are stronger. This is

due to the stators imposing a direct structural vibration on the wind tunnel's frame, while the vibrations related to the fan are vibrations in the airflow (the fan is not connected to the wind tunnel structure).

3. Model Vibration During Wind Tunnel Tests

Laser Vibrometer

Measurement locations with the laser vibrometer during live wind tunnel experiments are identical to those considered for the bump tests. Figure 16 (a) and (b) show the frequency response of the planar and C-wing configurations respectively at three angles of attack ($\alpha = 0^o$, 8^o, and 14^o). Frequency responses displayed have been averaged over five repeat experiments. Measurement locations are identical to those taken for bump tests in figure 11. The frequency response for both wing configurations, shown figure 16, are found to identify the same modal frequencies as the bump tests in figure 11(a). Further reiterating the findings from the bump tests suggesting the C-wing acted as a dynamic vibration absorber, figure 16 shows a significant attenuation of the wing vibrations. It is visible that the $7.2Hz$ peak present in the planar wing has been split into two frequency shifted peaks in the C-wing configuration, $5.3Hz$ and $11.8Hz$ respectively, in static wind tunnel testing. The split-peak arising from the side-wing/top-wing vibration interference is noticeable but could have been easily over looked and regarded as noise had bump testing not highlighted it's existence. Considering the first two dominant modes only ($1^{st}Mode$: $7.2Hz$ for planar; $5.3Hz$ for C-wing. $2^{nd}Mode$: $33.5Hz$ for planar; $33.2Hz$ for C-wing.), table III gives a summary of attenuation or amplification of the C-wing's main-wing vibrations relative to the planar wing.

TABLE III: Percentage change of the first two primary modes illustrating whether modal vibrations of the main-wing were attenuated or amplified by the C-wing relative to the planar wing.

α	1^{st} Mode [Δ%]	2^{nd} Mode [Δ%]
0^o	-25.22	+3.98
8^o	-7.46	-20.55
14^o	-68.63	-76.01

While there is a slight amplification of the second dominant mode at $\alpha = 0^o$ in tables III, all other cases show attenuation of the vibration amplitude. As separation over the upper side of the wing spreads, the wing will begin to buffet, the strength of which will increase with angle of attack. Notably, the C-wings ability to attenuate the main-wing vibrations improves as buffeting/separation worsens; attenuation of the fundamental mode is reduced by 68.63% at $\alpha = 14^o$.

From surface clay flow visualisations it is understood that the planar and C-wing share very similar stall characteristics. Buffeting results in a particular form of unsteady separation arising over a wing facilitating vibrations in the wing structure. Previous studies[65] have shown that the predominant buffet frequencies are expected to correspond to the fundamental bending frequency. This phenomenon is not critical for aircraft but does limit the flight envelope of commercial aircraft as the maximum allowable intensity of buffet is limited by regulations for passenger safety. Buffeting is additionally detrimental to the flying performance and manoeuvrability; if a reduction in the intensity of buffeting was applied to a commercial aircraft this would enable flight at higher altitude and increase the take-off weight.

Modern attempts to reduce buffeting are typically approached in two ways: 1) applying small static actions to control surfaces to slightly increase lift; 2) modifying the wing aerodynamics to avoid flow separation by adapting the wing profile or using mechanical vortex generators. The latter can be difficult to implement while only delaying buffet occurrence and does not reduce its intensity. In addition, aerodynamic modifications (such as mechanical vortex generators) are only effective in respect of buffeting of a specific nature and have been shown to increase drag in nominal cruise conditions[66]. There have been some attempts to actively reducing buffeting of swept wings in view of addressing a broad frequency spectrum, but these methods are complex, require instrumentation and power supply, and will add significant weight to the wing[67]. The findings of this study have shown that the C-wing has passively attenuates vibrations from buffet whilst simultaneously reducing total drag without a significant weight increase or root bending moment.

The C-wing dynamic vibration absorbency provided by the auxiliary mass (the top-wing) to the main vibrating system (the main-wing) can be described by the differential equations:

$$m_{mw}\ddot{X}_{mw} + R(\dot{X}_{mw} - \dot{X}_{tw}) + K_{mw}X_{mw} + K_{tw}(X_{mw} - X_{tw}) = F_o sin\omega_n t \qquad (9)$$

$$m_{tw}\ddot{X}_{tw} + R(\dot{X}_{tw} - \dot{X}_{mw}) + K_{tw}(X_{tw} - X_{mw}) = 0 \tag{10}$$

At frequencies well below resonance of the auxiliary mass, both masses move in phase and no vibration absorbency would be observed. Above its resonant frequency, the auxiliary mass provides an apparent fixed point in space which results in an opposing force being transmitted to the main-system. Through conservation of energy, the amplitude of displacement/velocity of vibration of the main system is reduced as kinetic energy is transferred to the auxiliary mass, thereby increasing the amplitude of displacement/velocity of vibration of the auxiliary mass[68]. The vibration of the auxiliary mass (the top-wing) moves out of phase with the main-wing. Therefore the elastic deformation of the side-wing is not only key for the transfer of forcing/kinetic energy, but also plays an important role in the mechanical impedance of the system and could be a structural point of failure if material fatigue is considered.

Figure 17 shows the frequency response of the C-wing's top-wing at three angles of attack ($\alpha = 0^o$, 8^o, and 14^o) under the same test conditions for the results in figure 16(b) and the same measurement location for bump tests shown in figure 11(b). The relative magnitude of the top-wing's peak vibrations relative to the main-wing's peak vibrations, shown in figures 17 and 16(b) respectively, are summarised in table IV.

TABLE IV: Percentage difference of the dominant vibration magnitude observed in the C-wing's top-wing relative to the C-wing's main-wing.

α	Change in peak vibration magnitude [Δ%]
0^o	+337.19
8^o	+183.83
14^o	+361.16

Due to the nature of the top-wing acting as a vibration absorber, and therefore absorbing kinetic energy from the main-wing, the dominant velocity magnitudes of the top-wing are significantly higher than that for the main-wing. At $\alpha = 14^o$ the velocity magnitude of the top-wing is noted to be 361.16% higher than that detected for main-wing structural vibrations.

It is appreciated that the induced vibration from buffeting are entirely different from gust loading and violent manoeuvres in a turbulent atmosphere with unsteady phenomena of short duration. Buffeting is induced by aero-elastic coupling between a constant source of excitation which can persist for long periods and has a stable and reproducible response. Consequently, particular flight conditions such as gusts do not occur under the same conditions, therefore the C-wing's vibration absorbency may not achieve the same level of attenuation.

Force Platform

It is necessary to consider how the interplaying vibrations influence the models' body forces and aerodynamic performance. Buffet results in lift and drag variations that greatly affect an aircraft's aerodynamics and impose limitations to the flight envelope. Here, $\alpha = 8^o$ has been taken as an example to demonstrate the variations in forces experienced by the model under static conditions. Figure 18(a) shows the raw drag coefficient (C_D) temporal response signal over a ten second period for both the planar and C-wing configurations. Figure 18(b) shows the frequency response of the sample data displayed in figure 18(a). The location of the force platform is shown in figure 18(d) for clarity.

The noise of both signals in figure 18(a) is considerable. Frequencies present in this signal, figure 18(b), show the wings' fundamental bending mode for both the planar wing and C-wing at approximately $9Hz$; this value is expected from previous bump tests on the fuselage shown in figure 14. The attenuation of this vibration is again observed. The force platform is also seen to detect frequencies at $44.2Hz$ and $253.2Hz$ which dominate that of the wing's primary vibrations. Coincidently the fuselage longitudinal natural resonant frequency of $39.9Hz$ (determined by bump tests in figure 14) is very close the $40.8Hz$ frequency of the wind tunnel's fan during operation at $Re = 1.5 \times 10^6$ (as seen in figure 15). This results in the excitation of the fuselage's longitudinal frequency thus significantly contributing to the noise detected along the x-axis of the force platform which is fixed to the longitudinal axis of the model. Secondary vibrations at $253.2Hz$ are found to be induced by the semi-span model's steel mounting interface as shown in figure 18(b). These vibrations are detected on all six force platform channels and represents a consequence of utilising a peniche-less semi-span model. This is not deemed to not out-way the benefits of removing the semi-span

model's peniche.

In order to negate the excited longitudinal fuselage and steel interface vibrations, which are not assumed to strongly influence the aerodynamic metrics, the force platform data was passed through a 10^{th} order $38Hz$ elliptical low-pass filter. The resulting temporal and frequency responses of this is shown in figures 18(c) and (d) respectively. The influence of removing the background noise in the temporal domain is unmistakable when comparing figures 18 (a) and (c). A summary of findings, comparing the mean, root mean squared (rms), and standard deviation (std) is given in table V. Here it is seen that the mean value of the drag coefficient between the filtered and unfiltered data remains unchanged. However, both the rms and std values of the signal reduce by approximately 5% and 68% respectively.

TABLE V: Summary comparing unfiltered and $38Hz$ low-pass filtered drag coefficient (C_D) data at $\alpha = 8^o$ over a ten second sample period from figures 18 (a) and (d) respectively.

	Unfiltered Signal			$38Hz$ Low-Pass Filtered Signal		
	mean(C_D)	rms(C_D)	std(C_D)	mean(C_D)	rms(C_D)	std(C_D)
Planar	0.0677	0.0721	0.0250	0.0677	0.0681	0.0079
C-wing	0.0621	0.0649	0.0190	0.0620	0.0624	0.0064

VI. CONCLUSIONS

An experimental investigation has been conducted to compare the performance of a semi-span planar wing and non-planar C-wing configuration at $Re = 1.5 \times 10^6$, including a detailed understanding of the model vibrations. Surface clay flow visualisations were used to compare flow over the wing indicating regions of attached/separated flows, stall fronts, stall cells, model surface imperfections, and horseshoe vortex interactions at the wing root. Aerodynamic performance metrics of each configuration were assessed using a force platform. Additionally, the model vibrations were evaluated and characterised using single-point laser vibrometry.

The surface clay flow visualisations identified the similarities in each wing configuration's stall characteristics, indicating that the C-wing's effects on stall over the main-wing are negligible. Assessment of each configuration's aerodynamic performance metrics showed that, despite the C-wings 19.1% increase in wing wetted area, an average total drag reduction

of 7.4% over a $0^o \leq \alpha \leq 14^o$ angle of attack range was achieved, *i.e.* where induced drag contribution to the total drag was dominant. A peak total drag reduction of 9.5% was reached at $\alpha = 6^o$. This is accomplished with the C-wing maintaining equivalent lift and root bending moment to that of the planar wing configuration. At negative angles of attack the total drag is seen to increase by up to 16.6% as parasitic drag dominates.

Furthermore, the C-wing's ability act as an undamped vibration absorber achieved a 68.63% attenuation of the excited primary bending mode due to buffet at $\alpha = 14^o$, relative to the planar wing. The C-wing's ability to passively maintain considerable drag reduction and vibration damping without significant increases in wing weight or root bending moment are promising. There are however structural limitations to the C-wing configuration, the primary limitations being: 1) inertial loading coupled with wing weight distribution; 2) the possibility of side-wing failure through material fatigue/inertial loading. The former was not an issue in this study as the wing was mounted vertically; however, it is necessary to highlight that this does understate the effect of gravity on the relatively heavier C-wing wingtip. The latter is a bi-product of the C-wing acting as an effective vibration absorber where is is seen the top-wing's dominant vibrational velocity magnitude is up-to 361.16% higher than that experienced by the main-wing.

It is also shown that forced vibrations from the wind tunnel excited the fuselage's natural frequency which translated to noisy interpretation of aerodynamic performance metrics. This is somewhat a consequence of a peniche-less semi-span model having less structural support and stiffness. However, with the characterisation of the model's natural frequencies a suitable $38Hz$ low-pass filter was implemented. This was found to reduce the force platform signal noise without significant changes to the mean signal values.

Acknowledgments

The authors would like to express our gratitude and appreciation to the low speed National Wind Tunnel Facility (EPSRC grant number: EP/L024888/1) at the University of Glasgow. Great appreciation must also be registered for Dr. Richard Green, whose support and technical expertise have been invaluable. The authors would also like to thank Dr. Andrea Cammarano for guidance in the vibrational analysis of vibration absorbers.

Finally, the authors would like to thank Zephyr Business Services and the Royal Aeronautical Society Centennial Scholarship for funding this work.

References

[1] European Commission. Flightpath 2050 Europe's Vision for Aviation.

[2] United States Aviation Greenhouse Gas Emissions Reduction Plan, 2015.

[3] J.E. Green. Civil Aviation and the Environment - The Next Frontier for the Aerodynamicist. *Aeronautical Journal*, 110(1110):469–486, 2006.

[4] F.A. Khan, P. Krammer, and D. Scholz. Preliminary aerodynamic investigation of box-wing configurations using low fidelity codes. *DGLR: Deutscher Luft-und ...*, 2010.

[5] A. Frediani. The Prandtl Wing. *VKI lectire series on Innivative Configurations and Advanced Concepts for Future Civil Aircraft*, pages 1–23, 2005.

[6] W. Schneider. The Importance of Aerodynamics in the Development of Commercial Successful Transport Aircraft. In Peter Thiede, editor, *Notes on Numerical Fluids Mechanics: Aerodynamic Drag Reduction Technologies*, volume 76. Springer, 2000.

[7] R.T. Whitcomb. A Design Approach and Selected Wind-Tunnel Results At High Subsonic Speeds For Wing-Tip Mounted Winglets. *NASA Technical Note: TN D-8260*, 1976.

[8] I. Kroo. Non-planar Wing Concepts For Increased Aircraft Efficiency. *VKI lectire series on Innivative Configurations and Advanced Concepts for Future Civil Aircraft*, pages 1–29, 2005.

[9] G. Kenway and J.R.R.A. Martins. Multipoint High-Fidelity Aerostructural Optimization of a Transport Aircraft Configuration. *Journal of Aircraft*, 51(1):144–160, 2014.

[10] T.F. Wunderlich. Multidisciplinary Wing Optimization of Commercial Aircraft With Consideration of Static Aeroelasticity. *CEAS Aeronautical Journal*, 6(3):407–427, 2015.

[11] G. Kenway and J.R.R.A. Martins. Aerodynamic Shape Optimization of the CRM Configuration Including Buffet-Onset Conditions. In *54th AIAA Aerospace Sciences Meeting, AIAA 2016-1294*, pages 1–23, San Diego, California, 2016.

[12] C.D. Cone. The Theory of Induced Lift and Minimum Induced Drag of Non-planar Lifting Systems. *NASA TR R-139*, 1962.

[13] J. DeYoung. Induced Drag Ideal Efficiency Factor of Arbitrary Lateral-Vertical Wing Forms: NASA CR-3357. Technical report, 1980.

[14] L. Demasi, A. Dipace, G. Monegato, P. Torino, and R. Cavallaro. Invariant Formulation for

the Minimum Induced Drag Conditions of Nonplanar Wing Systems. *AIAA Journal*, 52(10): 2223–2240, 2014.

[15] R.H. Liebeck, M.A. Page, and B.K. Rawdon. Blended-Wing-Body Subsonic Commercial Transport. *AIAA Paper 90-0438*, 1998.

[16] R.H. Liebeck. Design of the Blended Wing Body Subsonic Transport. *Journal of Aircraft*, 41 (1):10–25, 2004. ISSN 0021-8669. doi: 10.2514/1.9084.

[17] Z. Lyu and J.R.R.A. Martins. Aerodynamic Design Optimization Studies of a Blended-Wing-Body Aircraft. *Journal of Aircraft*, 51(5):1604–1617, 2014.

[18] J. McMasters, D. Paisley, R. Hubert, I. Kroo, K. Bofah, and J. Sullivan. Advanced Subsonic Configurations for Very Transport Airplanes Large. *NASA Contractor Report 198351*, 1996.

[19] J. Terry. Aerodynamic Charactaristics of Ring Wings: A Bibliography. *Redstone Scientific Information Center, Rept. RSIC-285*, 1964.

[20] L. Miranda. Boxplane Configuration for Conceptual Analysis and Initial Experimental Verification. *Lockheed California Co., Rept. LR 25180*, 1972.

[21] J. Wolkovitch. The Joined Wing: An Overview. *Journal of Aircraft*, 23:161–178, 1986.

[22] H.A. Lee, Y.I. Kim, G.J. Park, R.M. Kolonay, M. Blair, and R.A. Canfield. Nonlinear Response Structural Optimization of a Joined Wing Using Equivalent Loads. *AIAA Journal*, 44(4):1302–1308, 2007.

[23] R. Cavallaro and L. Demasi. Progress in Aerospace Sciences Challenges , Ideas , and Innovations of Joined-Wing Configurations : A Concept from the Past , an Opportunity for the Future. *Progress in Aerospace Sciences*, 87:1–93, 2016.

[24] M. Bhatia and R.K. Kapania. Structural and Aeroelastic Characteristics of Truss-Braced Wings : A Parametric Study. *Journal of Aircraft*, 49(1):302–310, 2012.

[25] I. Chakraborty, T. Nam, J.R. Gross, D.N. Mavris, J.A. Schetz, and K. Kapania. Comparative Assessment of Strut-Braced and Truss-Braced Wing Configurations Using Multidisciplinary Design Optimization. *Journal of Aircraft*, 52(6):2009–2020, 2015.

[26] W. Mallik, R.K. Kapania, and J.A. Schetz. Effect of Flutter on the Multidisciplinary Design Optimization of Truss-Braced-Wing Aircraft. *Journal of Aircraft*, 52(6):1858–1872, 2015.

[27] L. Prandtl. Induced Drag of Multiplanes. *Technical Report TN 182, NACA, Reproduction of Der induzierte Wilderstands von Mehreckern. technische Bar*, 3(7):309–315, 1924.

[28] M. Munk. *Isoperimetrische Aufgaben aus der Theorie des Fluges.* PhD thesis, Universitäts-

Buchdruckerei, 1919.

[29] P.J. Gage. *New Approaches to Optimisation in Aerospace Conceptual Design.* Phd. thesis, University of Stanford, 1994.

[30] L. Demasi, G. Monegato, A. Dipace, and R. Cavallaro. Minimum Induced Drag Theorems for Joined Wings , Closed Systems , and Generic Biwings : Theory. *Journal of Optimization Theory and Applications*, 169(1):200–235, 2016.

[31] L. Demasi, G. Monegato, E. Rizzo, R. Cavallaro, and A. Dipace. Minimum Induced Drag Theorems for Joined Wings , Closed Systems , and Generic Biwings : Applications. *Journal of Optimization Theory and Applications*, 169(1):236–261, 2016.

[32] L. Demasi. Investigation on the Conditions of Minimum Induced Drag of Closed Wing Systems and C-Wings. *Journal of Aircraft*, 44(1):81–99, 2007.

[33] P.W. Jansen, R.E. Perez, and J.R.R.A. Martins. Aerostructural Optimization of Nonplanar Lifting Surfaces. *Journal of Aircraft*, 47(5):1490–1503, sep 2010.

[34] I. Kroo, J. McMasters, and S.C. Smith. Highly Nonplanar Lifting Systems. *Transportation Beyond 2000: Technologies Needed for Engineering Design*, 1995.

[35] R. Slingerland and J.G. Verstraeten. Drag Characteristics for Optimally Span-loaded Planar, Wingletted, and C-Wings. pages 1–16, 2007.

[36] S.A. Ning and I. Kroo. Multidisciplinary Considerations in the Design of Wings and Wing Tip Devices. *Journal of Aircraft*, 47(2):534–543, 2010.

[37] H. Gagnon and D.W. Zingg. High-Fidelity Aerodynamic Shape Optimization of Unconventional Aircraft through Axial Deformation. In *52nd Aerospace Sciences Meeting, AIAA 2014-0908*, pages 1–18, National Harbor, Maryland, 2014.

[38] M. Trapani, M. PleiBner, A.T. Isikveren, and K. Weiczorek. Preliminary Investigation of a Self-Trimming Non-Planar Wing using Adaptive Utilities. *German Congress of Aeronautical Sciences*, 2012.

[39] A.T. Isikveren, A. Seitz, P.C. Vratny, C. Pornet, K. Plotner, and M. Hornung. Conceptual Studies of Universally-Electric Systems Architectures Suitable for Transport Aircraft. *German Congress of Aeronautical Sciences*, (April), 2012.

[40] U. Kling, C. Gologan, A.T. Isikveren, and M. Hornung. Aeroelastic Investigations of a Self-Trimming Non-Planar Wing. *German Congress of Aeronautical Sciences*, pages 1–9, 2013.

[41] K. Seywald, F. Hellmundt, A. Wildschek, and F. Holzapfel. Airworthiness Investigation of a

Highly Nonplanar Flexible Wing Concept. In *29th Congress of International Council of the Aerospace Sciences*, pages 1–10, St. Peterspurg, Russia, 2014.

[42] C. Suresh, K. Ramesh, and V. Paramaguru. Aerodynamic Performance Analysis of a Non-Planar C-wing Using CFD. *Aerospace Science and Technology*, 40:56–61, 2015.

[43] M. Gobpinaath, K. Sivajira, C. Suresh, and K. Ramesh. Design and Analysis of Non Planar Wing in Commercial Aircraft. *International Journal of Innovations in Engineering and Technology (IJIET)*, 7(3):472–485, 2016.

[44] J.D. Anderson. *Fundmentals of Aerodynamics*. McGraw-Hill, New York, 3rd edition, 2001.

[45] S.N. Skinner and H. Zare-Behtash. Semi-Span Wind Tunnel Testing Without Conventional Peniche. *Experiments in Fluids*, page IN PRESS, 2017.

[46] S.N. Skinner and H. Zare-Behtash. Aerodynamic Optimisation of Non-planar Lifting Surfaces. In *57th AIAA/ASCE/AHS/ASC Structures, Structural Dynamics, and Materials Conference, AIAA 2016-0164*, pages 1–21, San Diego, California, 2016.

[47] M.H. Shirk, T.J. Hertz, and T.A. Weisshaar. Aeroelastic Tailoring- Theory, Practice, and Promise. *Journal of Aircraft*, 23(1):6–18, 1986.

[48] O. Stodieck, J.E. Cooper, P.M. Weaver, and P. Kealy. Improved Aeroelastic Tailoring Using Tow-Steered Composites. *Composite Structures*, 106:703–715, 2013.

[49] D.H. Hodges and G.A. Pierce. *Introduction to Structural Dynamics and Aeroelasticity*. Cambridge University Press, second edi edition, 2011.

[50] C.M. Junior, D.C. Rebolho, E.M. Belo, and F.D. Marques. Identification of Flutter Parameters for a Wing Model. *Journal of the Brazillian Society of Mechanics, Science, and Engineering*, XXVIII(3):339–346, 2006.

[51] Y.C. Fung. *An Introduction of The Theory of Aeroelasticity*. Dover Publications, New York, first edit edition, 1993.

[52] T.H.G. Megson. *Aircraft Structures for Engineering Students*. Elsevier, fifth edit edition, 2013.

[53] E.H. Dowell. *A Modern Course in Aeroelasticity*. Fifth edit edition, 2014. ISBN 9783319094533. doi: 10.1007/978-3-319-09453-3.

[54] R.A. Wallis. Wind Tunnel Studies of Leading Edge Separation Phenomena on a Quarter Scale Model of the Outer Panel of the Handley Page 'Victor' Wing, with and without Nose Droop. Technical Report 3455, Ministry of Aviation, London, 1967.

[55] P.B.S. Lissaman. Low-Reynolds-Number Airfoils. *Annual Review of Fluid Mechanics*, 15:223–

239, 1983.

[56] J.B. Barlow, W.H. Rae, and A. Pope. *Low-Speed Wind Tunnel Testing*. John Wiley & Sons, ed., 3rd edition, 1999.

[57] K. Takenaka, K. Hatanaka, W. Yamazaki, and K. Nakahashi. Multidisciplinary Design Exploration for a Winglet. *Journal of Aircraft*, 45(5):1601–1611, 2008.

[58] AC. Webster and R. Vaicaitis. Application of tuned mass dampers to control vibrations of composite floor systems. *Engineering Journal of the American Institute of Steel Construction*, 29(3):116–124, 2003.

[59] A.R. Groh. The Dynamic Vibration Absorber Principle Applied to a High-Quality Phonograph Pickup. *Journal of The Audio Engineering Society*, 25(6):385–390, 1977.

[60] N. Jalili and N. Olgac. A Sensitivity Study on Optimum. *Journal of Vibration and Acoustics*, 122(2):1–8, 2000.

[61] S.F. Ali and S. Adhikari. Energy Harvesting Dynamic Vibration Absorbers. *Journal of Applied Mechanics*, 80(4):1–9, 2013.

[62] M. Tursun and E. Eskinat. H2 Optimization of Damped-Vibration Absorbers for Suppressing Vibrations in Beams With Constrained Minimization. *Journal of Vibration and Acoustics*, 136 (2):1–14, 2014.

[63] Y.I. Bobrovnitskii, K.D. Morozov, and T.M. Tomilina. Impedance Approach to Designing Efficient Vibration Energy Absorbers. *Acoustical Physics*, 63(2):141–147, 2017. ISSN 1063-7710.

[64] J.W. Hall and J.H. Grose. Some Effects of Auditory Grouping Factors on Modulation Detection Interference (MDI). *Journal of the Acoustical Society of America*, 90(6):3028–3035, 1991.

[65] D.M. Seal. A Survey of Buffeting Loads. Technical Report C.P. No. 584, Ministry of Aviation, 1962.

[66] P. Molton, J. Dandois, A. Lepage, V. Brunet, and R. Bur. Control of Buffet Phenomenon on a Transonic Swept Wing. *AIAA Journal*, 51(4):761–772, 2013.

[67] R. Destuynder, J. Bouttes, and P. Poisson-Quinton. Active Method and Installation for the Reduction of Buffetting of the Wings of an Aircraft, 1987.

[68] H. Jo and H. Yabuno. Amplitude Reduction of Primary Resonance of Nonlinear Oscillator by a Dynamic Vibration Absorber Using Nonlinear Coupling. *Nonlinear Dynamics*, 55(1-2):67–78, 2009.

List of Figures

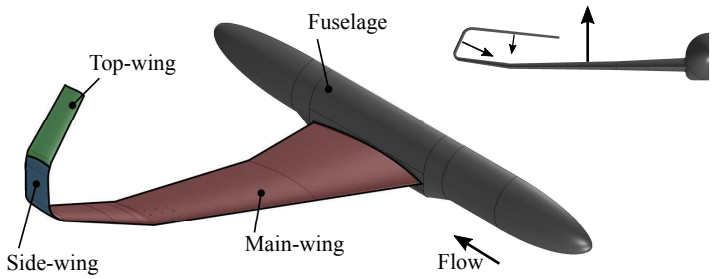

FIG. 1: C-wing layout with positive direction of span-loading on each surface indicated.

(a)Planar wing semi-span model.

(b)C-wing semi-span model.

FIG. 2: Semi-span models in wind tunnel working section.

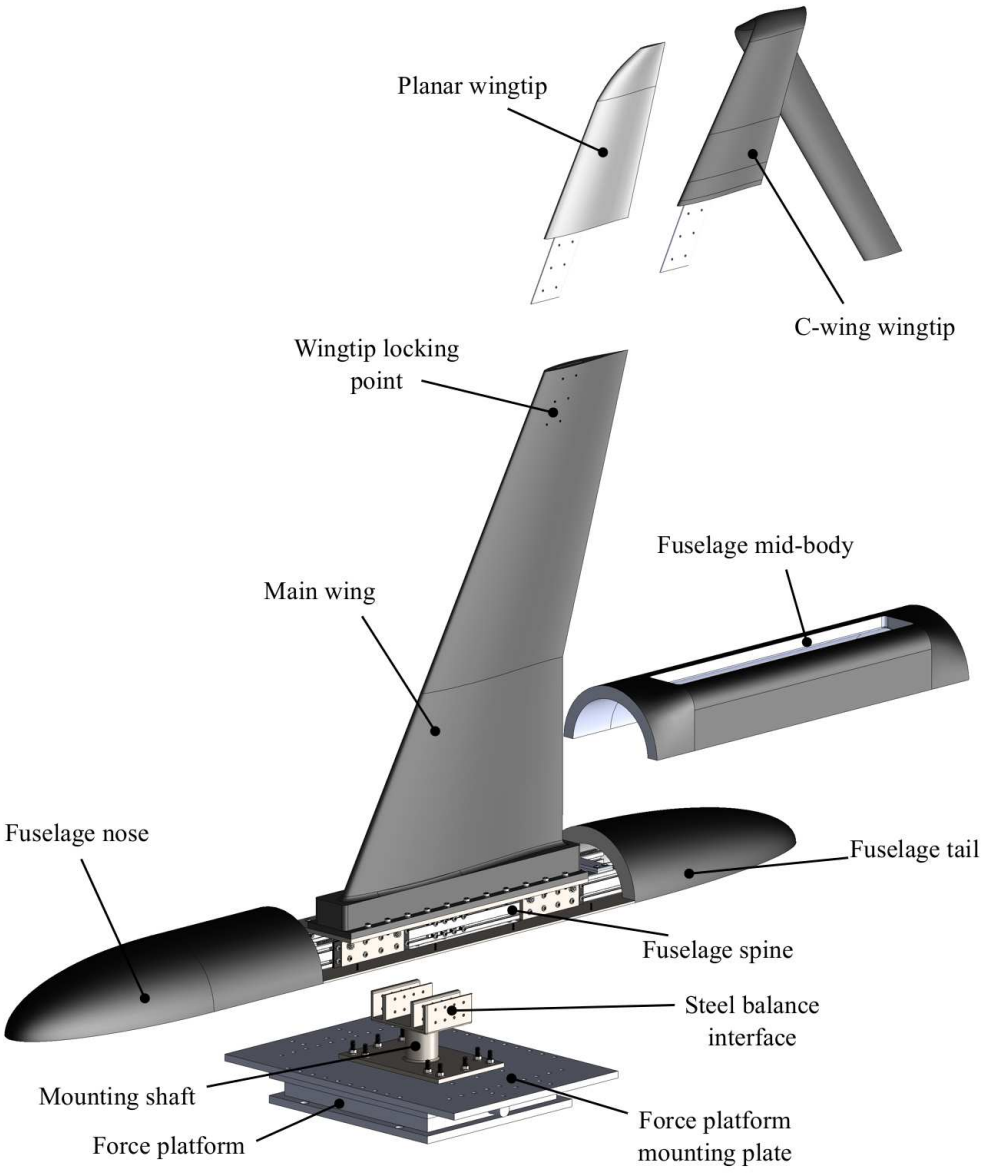

FIG. 3: Exploded view of model.

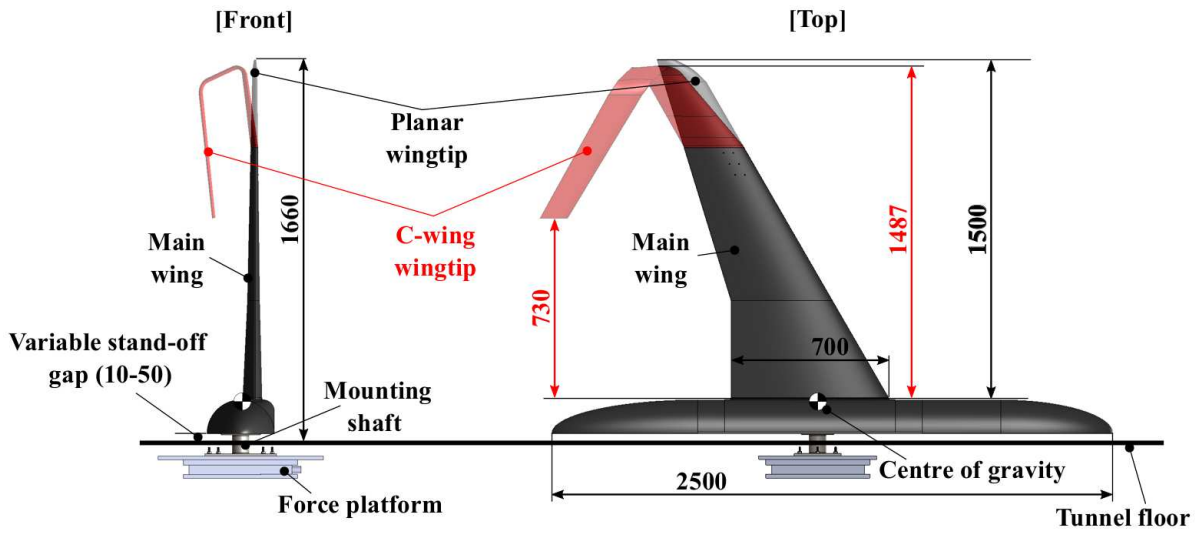

FIG. 4: Semi-span model schematic diagram; dimensions are in [mm].

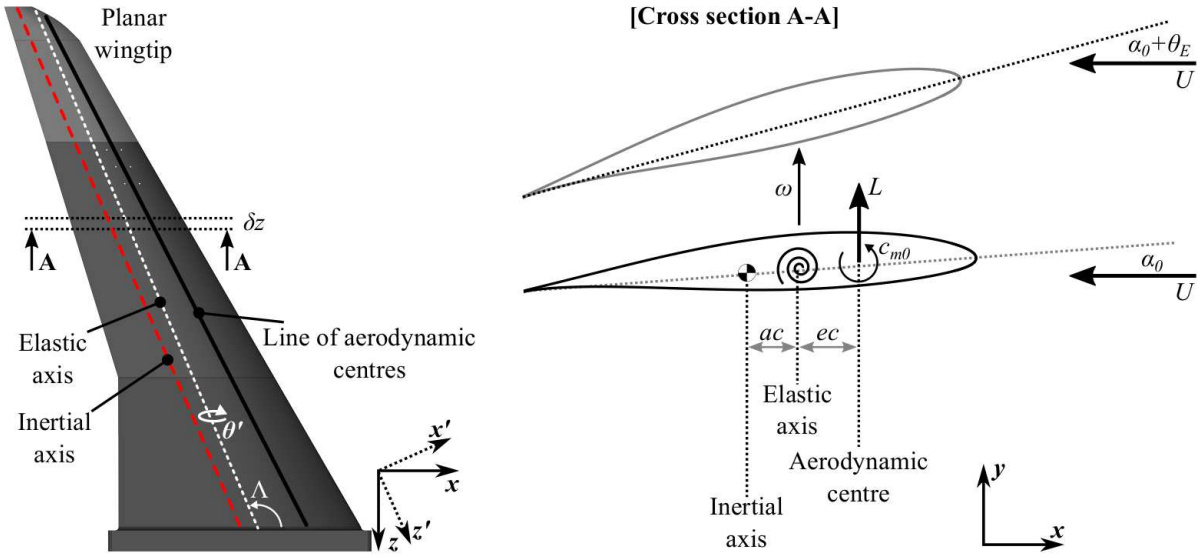

FIG. 5: Typical aerodynamic, elastic, and inertial axes of a swept planar wing with aerodynamic coupling ec, and inertial coupling ac resulting in coupled bend-twist wing deformation.

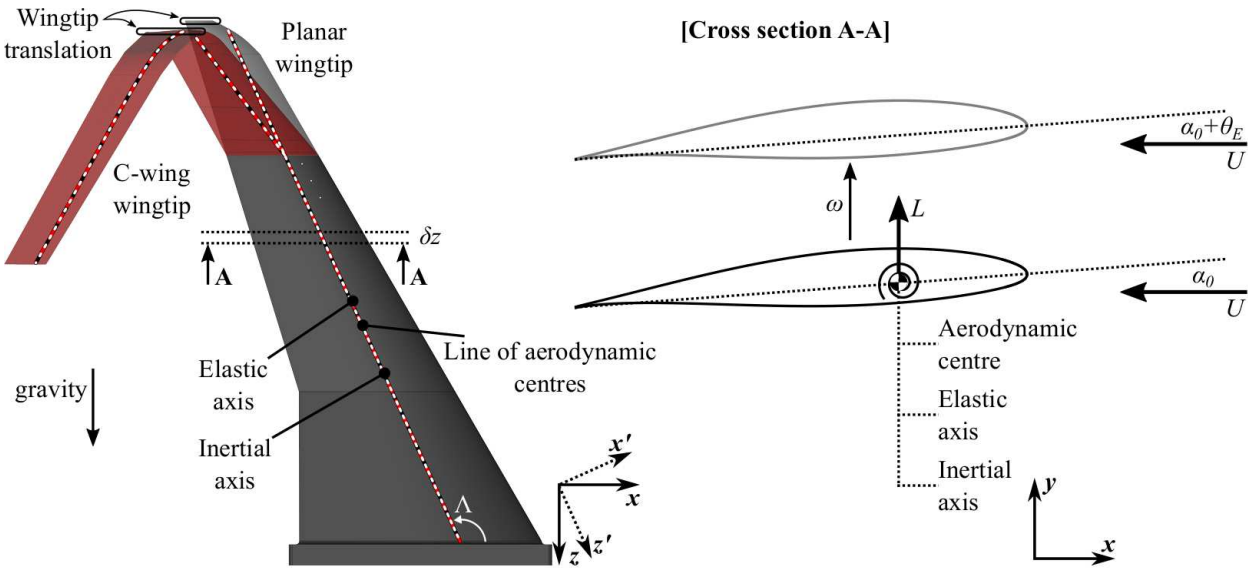

FIG. 6: Aligned aerodynamic, elastic, and inertial axes to de-couple bend-twist deformation.

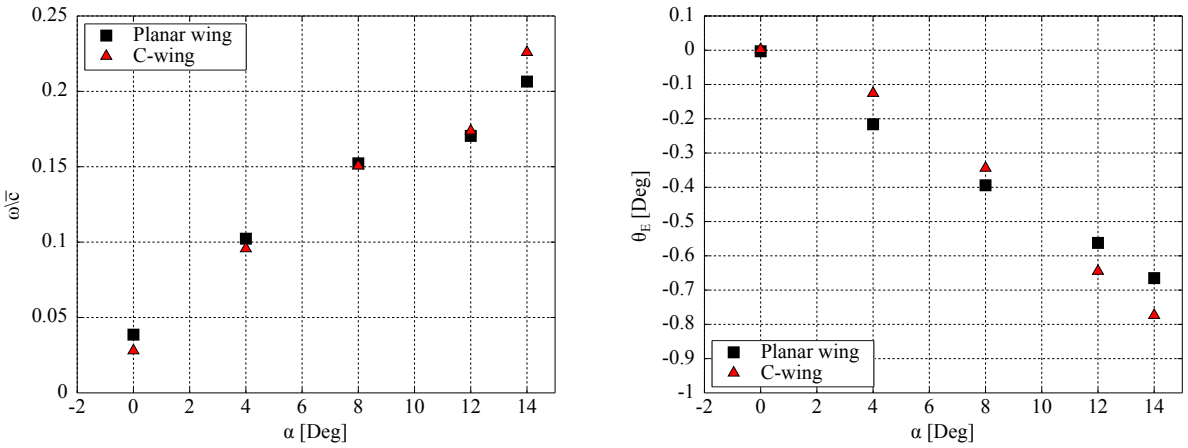

(a)Mean wingtip translation.

(b)Mean wingtip rotation.

FIG. 7: Planar and C-wing main wing wingtip translation and rotation with angle of attack at $Re = 1.5 \times 10^6$.

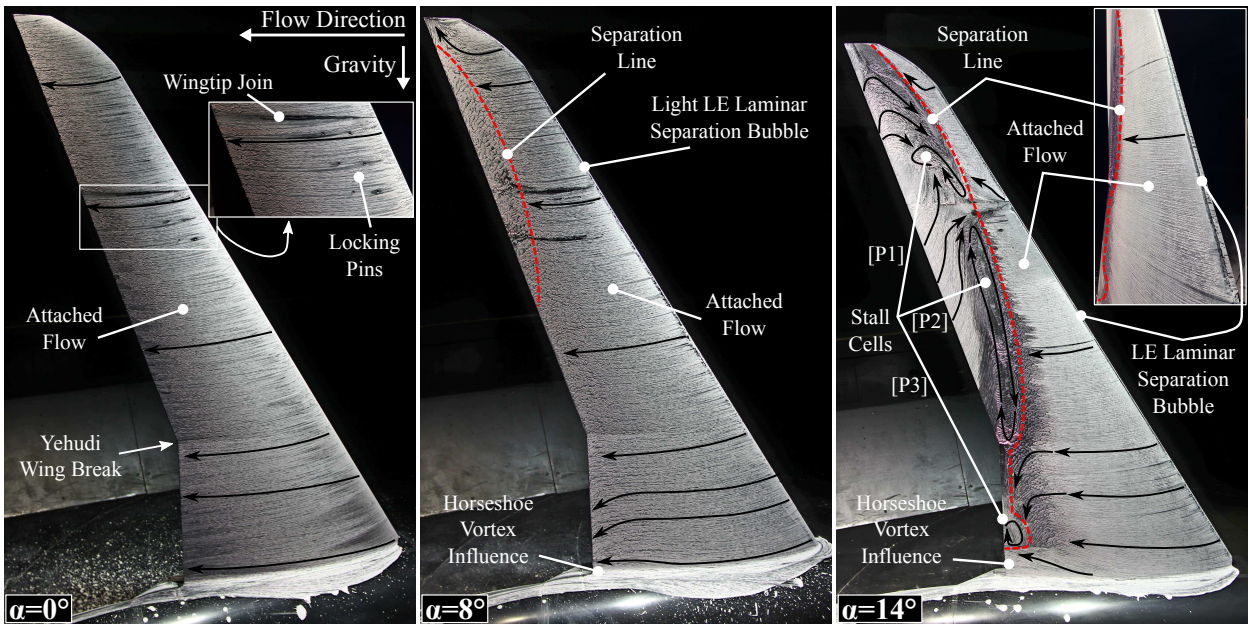

(a)Planar wing.

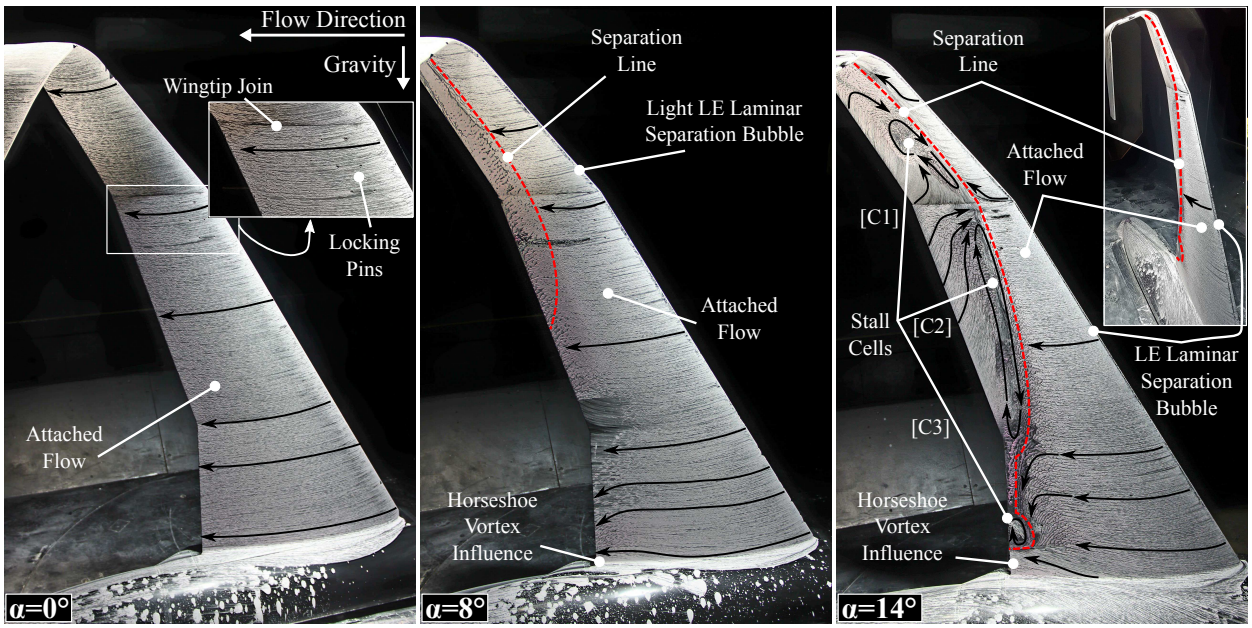

(b)C-wing's main-wing section.

FIG. 8: Surface clay flow visualisation over the planar and C-wing configurations at $Re = 1.5 \times 10^6$ for $\alpha = 0^o$, 8^o, and 14^o.

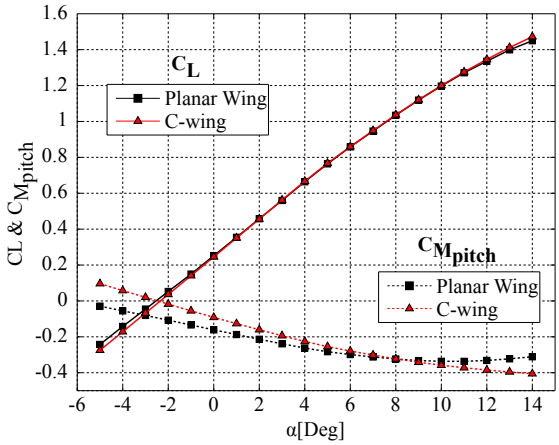

(a)$C_L - \alpha$ & $C_{M_{pitch}} - \alpha$

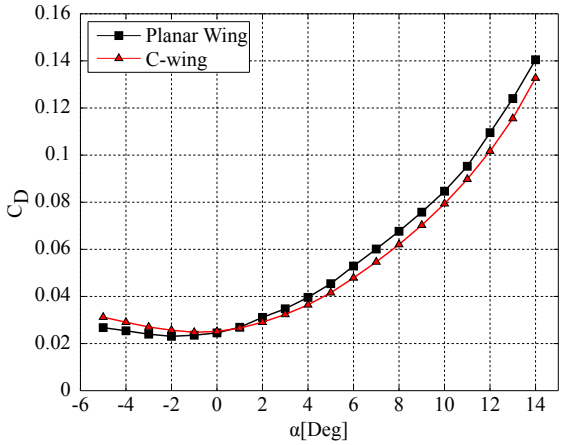

(b)$C_D - \alpha$

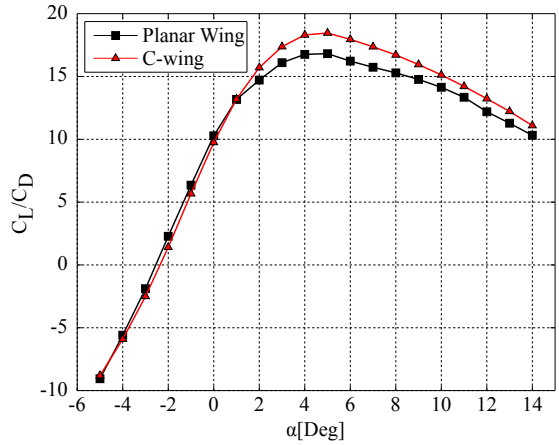

(c)$C_L/C_D - \alpha$

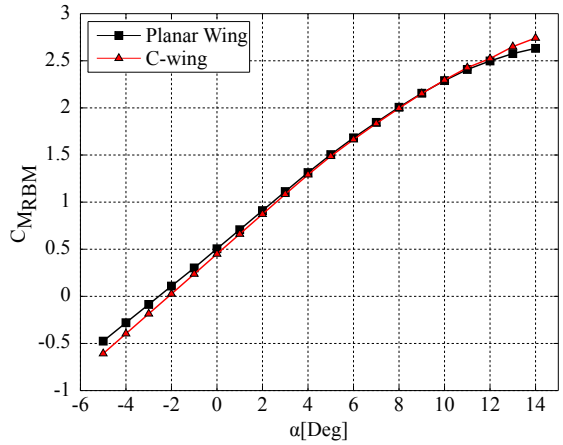

(d)$C_{M_{RBM}} - \alpha$

FIG. 9: Aerodynamic Coefficients for the planar wing and the C-wing.

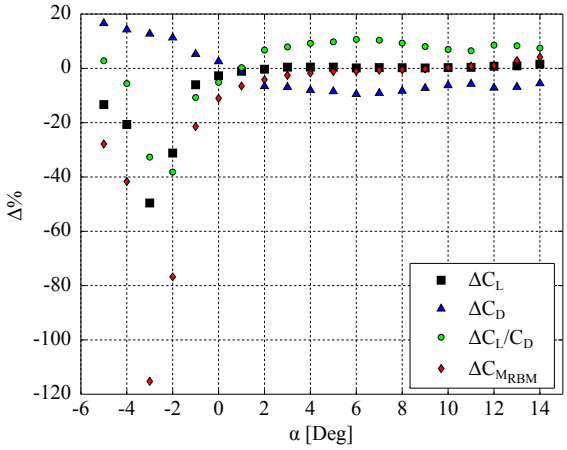

FIG. 10: Percentage change of C-wing arrangement aerodynamic coefficients relative to planar arrangement.

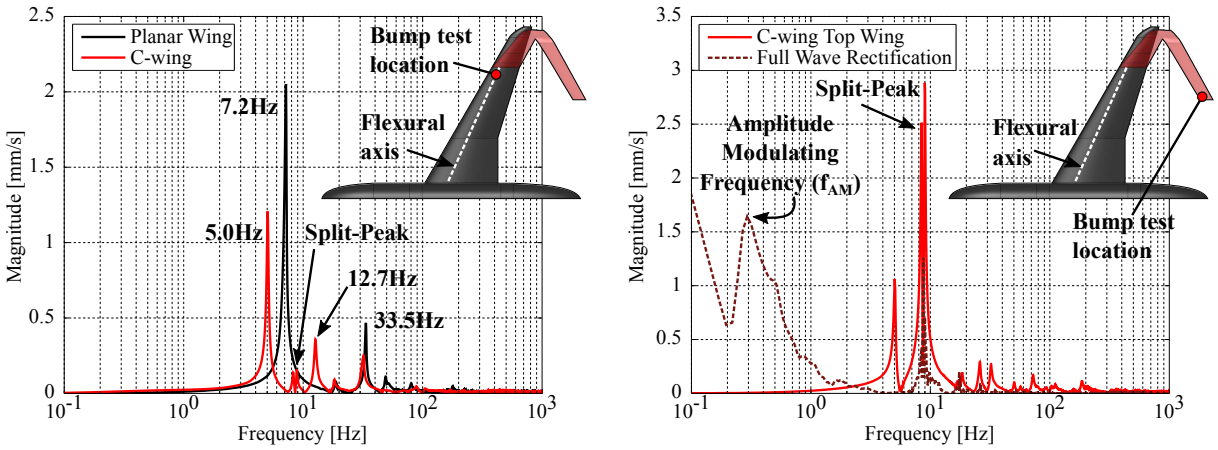

(a)Frequency response for planar and C-wing main-wing; bump test location indicated.

(b)Frequency response for C-wing's top-wing wingtip; bump test location indicated.

FIG. 11: Bump test frequency response of wing configurations observed with 1-D laser vibrometer.

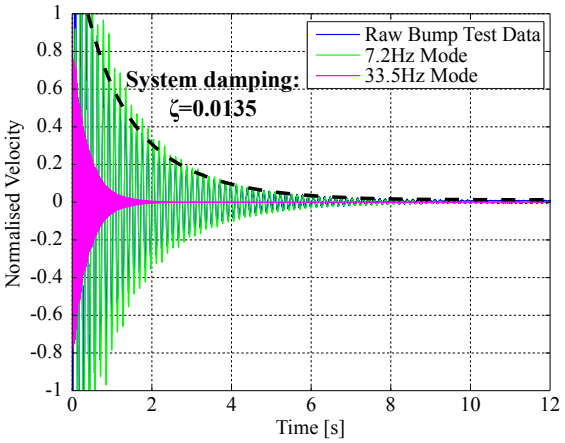

(a)Temporal response from planar wing bump test; bump test location shown in figure 11(a).

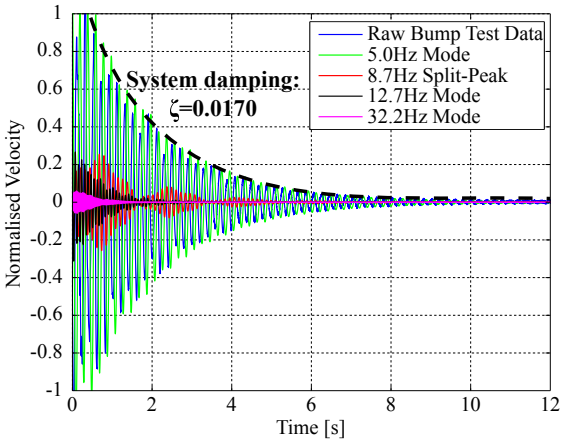

(b)Temporal response from C-wing wing bump test; bump test location shown in figure 11(a).

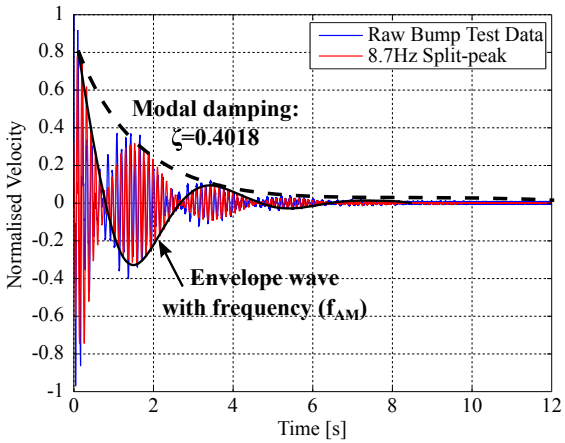

(c)Temporal response from C-wing top-wing bump test; bump test location shown in figure 11(b).

FIG. 12: System and dominant mode temporal responses of wing configurations undergoing bump tests. Bump test location and dominant modal frequencies are indicated in figure 11.

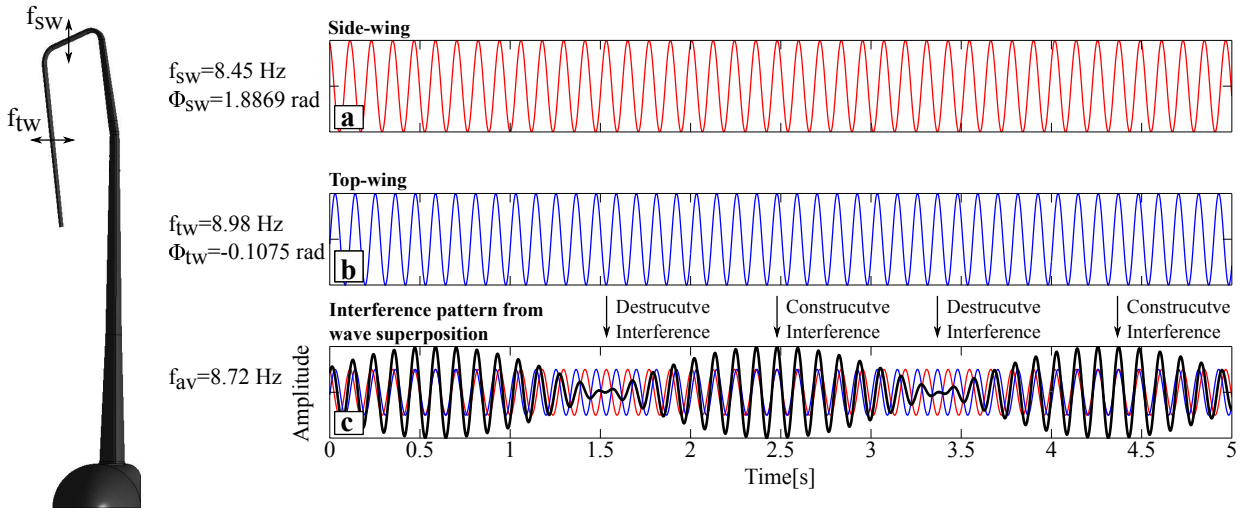

FIG. 13: Explanation of beating interference pattern observed from interaction of side-wing and top-wing vibrations.

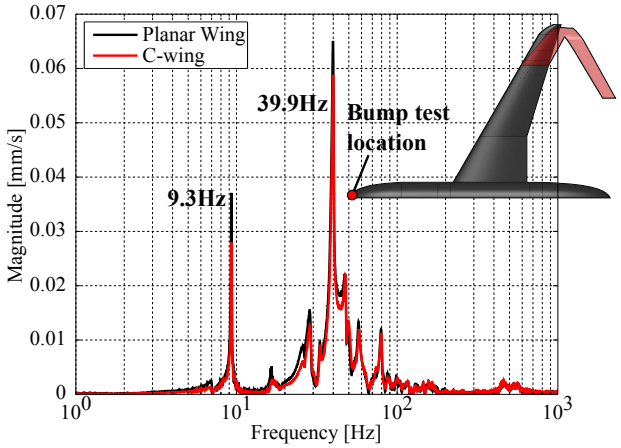

FIG. 14: Frequency response observed in the longitudinal fuselage axis; bump test location indicated on the model fuselage.

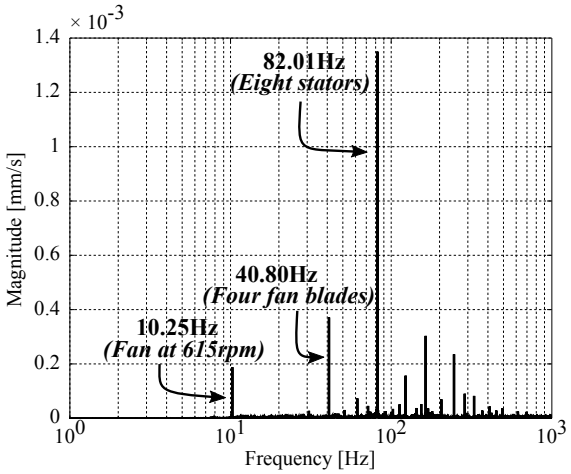

FIG. 15: Frequency response, detected by laser vibrometer, of the exterior steel frame of the empty working section at a Reynolds number of 1.5×10^6 based on the wing MAC.

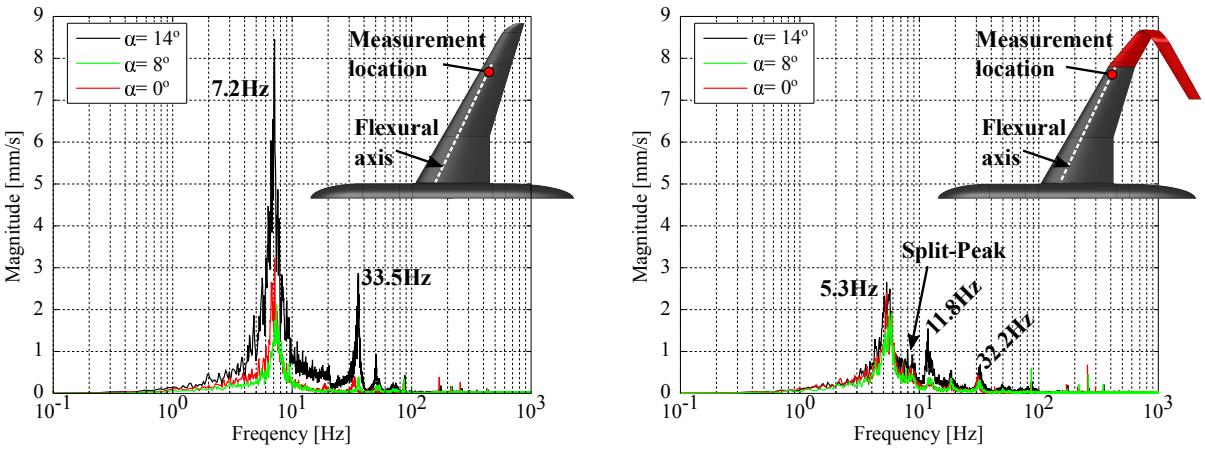

(a)Planar wing. (b)C-wing.

FIG. 16: Frequency response, detected by laser vibrometer, of wing configurations at $\alpha = 0^o$, 8^o, and 14^o, at a Reynolds number of 1.5×10^6 based on the wing MAC; the indicated measurement location is that same as that shown in figure 11(a).

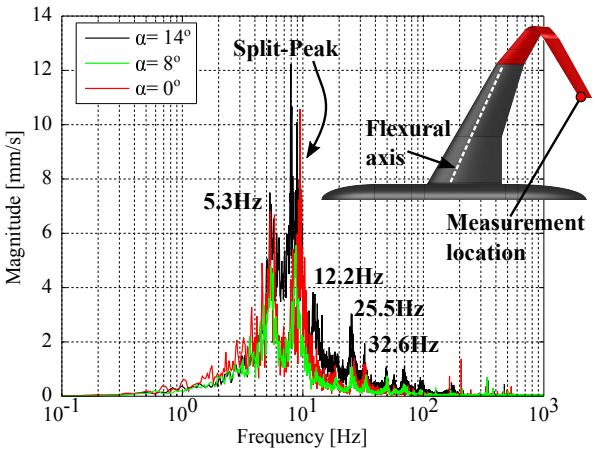

FIG. 17: Frequency response, detected by laser vibrometer, of the C-wing's top -wing wingtip at $\alpha = 0^o$, 8^o, and 14^o, at a Reynolds number of 1.5×10^6 based on the wing MAC; measurement location indicated.

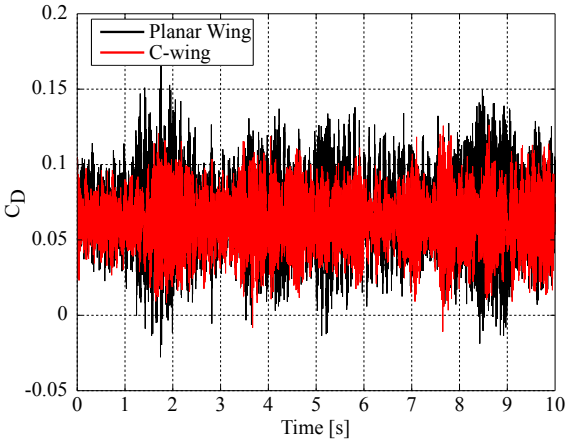

(a)Unfiltered C_D temporal response.

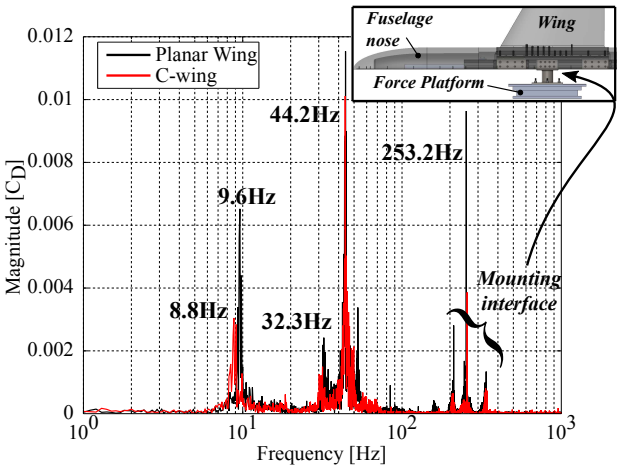

(b)Unfiltered C_D frequency response.

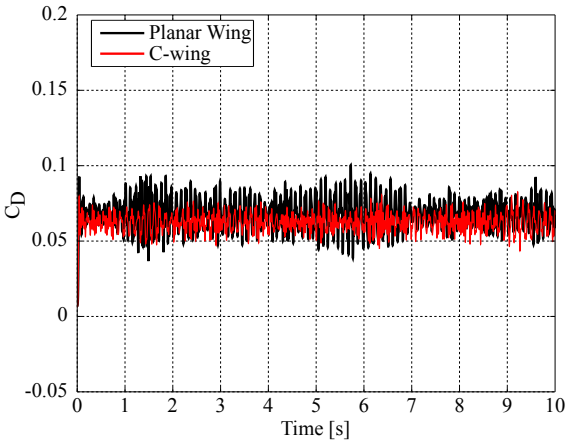

(c)$38Hz$ low-pass filtered C_D temporal response.

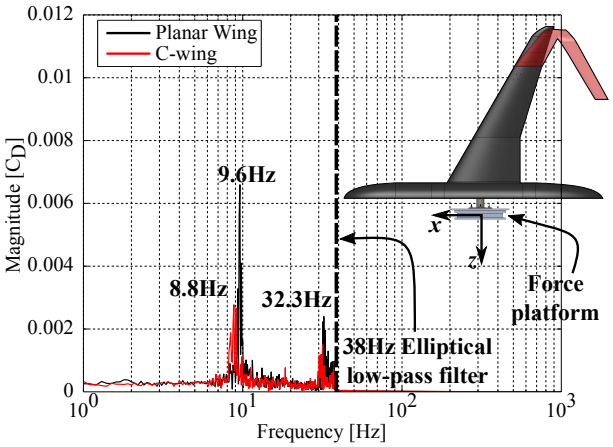

(d)$38Hz$ low-pass filtered C_D frequency response.

FIG. 18: Drag coefficient recorded by force platform for both the planar and C-wing configurations at $\alpha = 8^o$ for $Re = 1.5 \times 10^6$; $38Hz$ low-pass filtered and unfiltered data presented.